PAPER

Plasma catalysis: separating plasma and surface contributions for an $Ar/N_2/O_2$ atmospheric discharge interacting with a Pt catalyst

To cite this article: Michael Hinshelwood and Gottlieb S Oehrlein 2023 *Plasma Sources Sci. Technol.* **32** 125001

IOP Publishing Plasma Sources Science and Technology
Plasma Sources Sci. Technol. **32** (2023) 125001 (20pp) https://doi.org/10.1088/1361-6595/ad0f47

Plasma catalysis: separating plasma and surface contributions for an $Ar/N_2/O_2$ atmospheric discharge interacting with a Pt catalyst

Michael Hinshelwood and Gottlieb S Oehrlein*

Department of Materials Science and Engineering and the Institute for Research in Electronics and Applied Physics, University of Maryland, College Park, MD 20742, United States of America

E-mail: oehrlein@umd.edu

Received 15 September 2023, revised 14 November 2023
Accepted for publication 23 November 2023
Published 6 December 2023

Abstract

Atmospheric pressure non-equilibrium plasmas can form nitrogen oxide (NO_x) compounds directly from nitrogen and oxygen without a catalyst, and at lower catalyst temperatures than would be possible without plasma. In this work, the oxidation of plasma-produced NO from an $Ar/N_2/O_2$ non-equilibrium atmospheric-pressure plasma-jet (APPJ) over a platinum-on-alumina powder catalyst was investigated with *in-situ* infrared spectroscopy. Products downstream of the catalyst bed were analyzed along with catalyst surface species. The catalyst was exposed to plasma at both constant temperature and a cyclic temperature ramp in order to study long-lasting and transient surface changes. Primary incident reactive species to the catalyst were assessed to be NO and O_3. Pt-Al_2O_3 at 350 °C increased oxidation of NO relative to Al_2O_3 or an empty chamber. The surface state of Pt-Al_2O_3 evolves during plasma-effluent exposure and requires upwards of 20 min exposure for stabilization compared to Al_2O_3. Once stable surface conditions are achieved, thermal cycling reveals a repeatable hysteresis pattern in downstream products. At low temperature, oxygen and NO_x accumulate on the catalyst surface and react at elevated temperatures to form NO_2. Increasing plasma power and O_2:N_2 ratio increases the hysteresis of the heating relative to the cooling curves in the pattern of NO_2 formation. The limitation on NO oxidation at high temperatures was assessed to be Pt-O which is depleted as the catalyst is heated. Once stored species have been depleted, NO oxidation rates are determined by incoming reactants. Two overlapping NO oxidation patterns are identified, one determined by surface reactants formed at low temperature, and the other by reactants arriving at the surface at high temperature. The plasma is responsible for providing the reactants to the catalyst surface, while the catalyst enables reaction at high temperature or storage at low temperature for subsequent reaction.

Keywords: plasma, catalysis, atmospheric pressure, NO_x

1. Introduction

Nitrogen fixation, the conversion of stable N_2 into reactive nitrogen species, is essential for production of artificial fertilizers for large-scale agriculture. The preeminent method of nitrogen fixation is the Haber–Bosch process for synthesizing ammonia using N_2 and H_2, where H_2 is derived from CH_4 via the reverse water gas shift reaction [1]. The Haber Bosch process is carbon intensive, responsible for 2% of emissions worldwide per year [2]. Thus, green nitrogen fixation, the ability to create reactive nitrogen compounds

* Author to whom any correspondence should be addressed.

with carbon-free energy generation technologies, has become a topic of high interest in recent years.

Many advanced catalytic techniques are being evaluated, such as electrocatalysis [3, 4] or photocatalysis [5]. One promising method is plasma catalysis [6]. Plasma catalysis, the coupling of a plasma with a heterogenous catalytic reaction, is being researched for several different applications including air treatment [7], methane decomposition [8], and nitrogen fixation, and shows promise for enhancing the catalytic yield [9]. Plasma catalysis also opens the door for reactions at atmospheric pressure, which is attractive for large-scale production.

In plasma catalysis, the plasma creates a variety of excited gas species, electronically excited species, atomic radicals, ions, electrons, photons, or intermediate gas compounds [10]. These species may interact with the catalyst and lower the activation energy of reactions or improve product yields [8]. With the wide variety of species potentially arriving at the catalyst surface, the interactions occurring can be complex. The plasma may also contribute in other ways, such as surface heating or catalyst morphology changes [11, 12]. Some studies have demonstrated a synergistic effect, where the sum of products created by the plasma and created by thermal catalysis alone is less than when the plasma is coupled with a catalyst [1]. Lasting surface changes, which result in improved catalytic performance even after the plasma is turned off, have also been observed [13].

Plasma catalysis for nitrogen fixation has been focused on two reactions, N_2 and H_2 to form NH_3 and N_2 and O_2 to form nitrogen oxides (NO_x). Both can contribute to fertilizer creation through the formation of nitrates [14]. In this work we focus on the latter.

The formation of NO_x by plasma alone is a well-known process and has been investigated for the production of fertilizers as far back as 1903 with the invention of the Birkeland–Eyde process [15]. Oxidation of N_2 in the gas phase takes place through the Zeldovich mechanism, with N reacting with O_2 or O reacting with N_2 [16]. Without the presence of plasma this takes place at the surface of a catalyst at high temperature and pressure. With plasma, atomic N and O can be created through electron impact dissociation at atmospheric pressure, allowing for NO formation at more favorable conditions. Research efforts are still ongoing into efficient plasma generation systems to create NO_x directly in the plasma [16–18].

Recently, plasma catalytic formation of NO_x has been explored to improve on pure plasma formation. Ma *et al* demonstrated a significant enhancement of NO formation with a Pt-Al_2O_3 catalyst at lower pressures (3 torr), which was attributed to the dissociation of vibrationally excited nitrogen on the catalyst surface [19]. However, it is unclear if such processes take place at atmospheric pressure. NO_x formation through plasma catalysis has been demonstrated by Patil *et al* with a packed bed dielectric barrier discharge and various metal oxide powders [20]. They demonstrated that the catalyst power can influence the plasma by creating micro discharges that increase the product formation but did not find evidence of enhanced N_2 cracking on the catalyst surface [20].

Direct analysis of reactions on the catalyst surface have remained scant. This is due to the difficulties imparted by plasma–catalyst interaction at atmospheric pressure [21]. For packed bed reactor systems, incorporating a diagnostic is technically difficult. Additionally, many standard techniques for surface science require high vacuum, precluding their use with atmospheric pressure plasma [21]. Thus, a detailed understanding of the surface reactions is still required for many plasma catalyst interactions. This necessitates the ability to separate the contribution of the plasma and the catalyst to any given reaction. For the interaction of N_2/O_2 based plasmas with catalysts at atmospheric pressure, it is still unclear how the plasma influences reactions on the catalyst surface, and what contributions to the overall reaction are due to the plasma or the catalyst.

In this work, we employ a reactor developed by Knoll *et al* which allows for *in-situ* surface characterization of the catalyst under plasma exposure [22]. We investigated the coupling of a N_2/O_2 atmospheric pressure plasma over a Pt-Al_2O_3 catalyst for the oxidation of N_2. The catalyst is compared to bare support material and an empty chamber to understand its contribution to the interaction and products. An overview of the coupling at constant catalyst temperature is presented first, followed by a description of coupling when the catalyst temperature is cycled so that any changes to catalyst performance may be identified. By comparing the coupling with constant catalyst temperature or thermal cycling the individual roles of plasma or catalyst are separated. Additionally, transient, and long-lasting catalyst alterations are effectively separated. These findings provide a valuable method for effectively studying plasma–catalytic reactions and separating transient surface changes from long-lasting ones that may lead to catalyst activation.

2. Experimental design

2.1. Plasma source

The plasma jet used in this work is an annular-ring type dielectric-barrier discharge atmospheric pressure plasma jet (APPJ) developed by Zhang *et al* [23] and is illustrated in figure 1, along with the entire experimental setup. It consists of a 1 mm tungsten pin inserted into a quartz tube with interior diameter of 3 mm. A copper ring placed around the end of the quartz tube serves as the ground electrode. The characteristics of this jet have been thoroughly detailed [23–25]. In this work, the plasma jet was fed with a feed gas of N_2 and O_2 backed by Ar. The jet is operated at 14.3 MHz with a duty cycle of 20%. This operating frequency was found in prior work to maximize power dissipation in the plasma for this APPJ with similar gas flow conditions [8].

Two gas compositions were primarily used in the work described here. The first with an N_2/O_2 ratio similar to air; 2.5 sccm N_2, 0.5 sccm O_2, and 200 sccm Ar. The second with a higher O_2 percentage, 0.5 sccm N_2, 2.0 sccm O_2, and 200 sccm Ar. These will be termed as N_2 rich and O_2 rich respectively for the rest of this work. Under both conditions, the plasma was

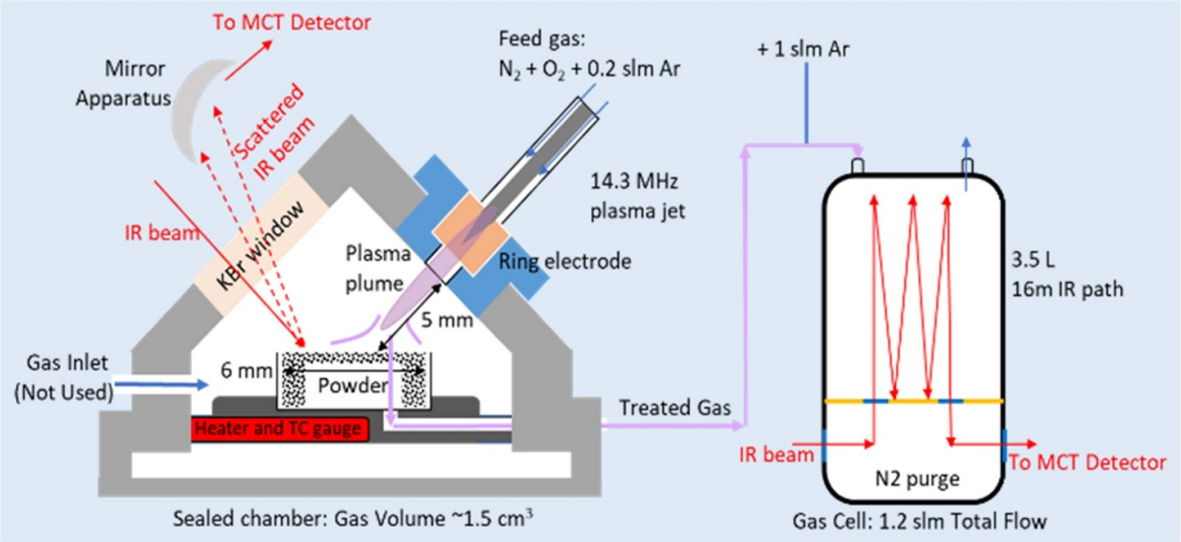

Figure 1. Plasma catalyst reactor diagram. Nozzle orifice to powder distance is 5 mm.

operated primarily at 2 W. Plasma power in this work refers to the power dissipated in the plasma, which was calculated by subtracting the stray power from the total power in the circuit. This technique has been previously detailed in work by Li *et al* [8].

2.2. Reaction chamber and catalyst

The reaction chamber in this work is a modified high temperature reaction chamber (Harrick Scientific) which has been previously described [8, 22]. The chamber has a total internal volume of approximately 1.5 cm^{-3} and houses a stainless-steel cup to hold catalyst powder. The catalyst cup can be heated from below and the temperature is monitored with a thermocouple. The chamber itself is water cooled. The reactor lid has two openings. One of these openings houses a window for diffuse reflectance infrared Fourier transform spectroscopy (DRIFTS) measurements. The other opening features a ceramic feed through which holds the end of the APPJ (see figure 1). Gas flows through the plasma jet and towards the catalyst located 5 mm from the orifice. The composition of the flux of plasma-generated reactive species depends on operating conditions. At the flow rates employed in this work (200 sccm) the time it takes a gas species to travel from the nozzle to the powder surface is estimated to be around 40 ms. After passing through the catalyst bed, the gas flows out of the reaction chamber carrying any formed products with it. Unexcited gas may also be flowed through ports in the reaction chamber; however, this was not employed in this work.

In this work, 5 wt% Pt on γ-Al_2O_3 catalyst was used. The catalyst was purchased from Sigma Aldrich, product number 205974. Characterization of the same product number by Chen *et al* and Engelbrecht *et al* indicate that this catalyst has a surface area of $\sim$100 m^2 g^{-1} with a pore size of $\sim$9 nm and a Pt particle diameter of $\sim$5 nm [26, 27]. The surface area characteristics of the bare Al_2O_3 material are unknown. The Al_2O_3 particle size for both Pt-Al_2O_3 and Al_2O_3 was assessed to be between 37 and 74 μm in diameter through sieving. Stainless-steel mesh was used to prevent catalyst powder from falling through the bed outlet.

2.3. Downstream gas and in-situ operando surface analysis

Plasma–catalyst interactions were analyzed in one of two ways, catalyst surface characterization or characterization of gas species downstream of the plasma–catalyst interaction. *In-situ* operando surface characterization was carried out with a DRIFTS compartment (Harrick scientific) to which the reaction chamber was inserted. The entire apparatus is located in an FTIR spectrometer (Shimazdu, IR-Tracer 100) which is fitted with a high sensitivity MCT (MgCdTe) detector. Two KBr windows on the reaction chamber lid allow for IR light to pass through. Changes in IR absorbance patterns can be ascribed to adsorbed species on the catalyst surface. DRIFTs spectra were recorded with 4 cm^{-1} resolution, with a 20 scan average for a good balance of signal sensitivity to noise. As the exact calibration factors for surface species coverage to signal intensity was not known, DRIFTS analysis is only qualitative.

Characterization of downstream gas species was performed with the same FTIR spectrometer equipped with a high sensitivity, 16 m path-length gas cell (Pike Technologies). Gas from the reaction chamber outlet flowed through 30 cm of tubing before mixing with a stream of 1 slm Ar to reduce the residence time within the gas cell. This mixture then flowed along another 80 cm of tubing before entering the gas cell, for a total transfer time between reactor and measurement cell of around 2 s. FTIR spectra were recorded at higher resolution, 0.5 cm^{-1} resolution, with 10 scans averaging. Gas species densities were quantified using species IR cross-section data taken from the HITRAN database [28]. Both DRIFTS and downstream FTIR spectra were taken in real time. Since only one measurement can be performed at a time, every experiment was performed

twice. Prior to performing any experiment (DRIFTS or downstream gas), gas lines were evacuated to 10^{-5} torr, and the reaction chamber was purged with Ar for 30 min to minimize interference due to water or other impurities.

The nature of the experimental setup means that immediate reactive species flux to the catalyst surface has not been quantified. However, results from the literature with similar plasma generation devices are drawn upon to qualitatively inform how reactive species fluxes may shift between different experimental conditions. Details are covered in section 4.1.

For experiments involving thermal cycling, the powder bed was initially exposed to plasma for 5 min at 100 °C to ensure stability of the powder surface. It was then heated under plasma exposure from 100 °C to 350 °C at 10 °C min^{-1} with a 1 min dwell time at end temperatures to compensate for small overshoots in the set temperature. For all experiments, the catalyst was not heated beyond 350 °C. This was to avoid the formation of gaseous platinum oxide, which could redeposit further down the gas lines, contaminating the set-up. Oxide in bulk typically does not sublimate below 800 °C [29, 30], but nanoparticles may form gaseous PtO at 400 °C [31, 32].

3. Experimental results

3.1. Analysis of downstream gas-phase products

Gas phase characterization was performed to understand how the coupling of the plasma with catalyst influences the plasma products. First, the species produced in an empty chamber were analyzed, to gain an understanding of what is created in the plasma. Next the catalyst was exposed to the plasma at constant temperature, to understand how downstream species evolve with time. Finally, the catalyst was thermal cycled under plasma exposure to help separate the contribution of plasma and catalyst to the product densities.

3.1.1. Overview of gas-phase products. Gas phase characterization was performed to determine and quantify products produced by the plasma–catalytic reaction. Figure 2 shows an example of an FTIR spectrum of downstream gas products during exposure of the empty chamber to plasma of various powers and feed gas compositions. These spectra were recorded with the catalyst temperature at 25 °C. Only three downstream IR visible reactive oxygen–nitrogen species (RONS) are visible at the conditions shown: NO_2, NO, and N_2O. Other species such as O_3, N_2O_5, and HNO_3 appear at lower power for O_2 rich conditions, however their spectral profile is not shown here. Spectral features were converted into densities through Beer's law, shown in equation (3.1),

$$A = xlC \tag{3.1}$$

where C is the concentration, x the IR cross section, A absorbance, and l is the total IR path length.

IR cross sections for the respective species were obtained through the HITRAN database [28]. Error in the relative shift in densities of a compound is very small. However, as the gas densities were not calibrated with calibration gas, error may be present in the quantification. Thus, discussion in this paper primarily focuses on relative shifts in product densities.

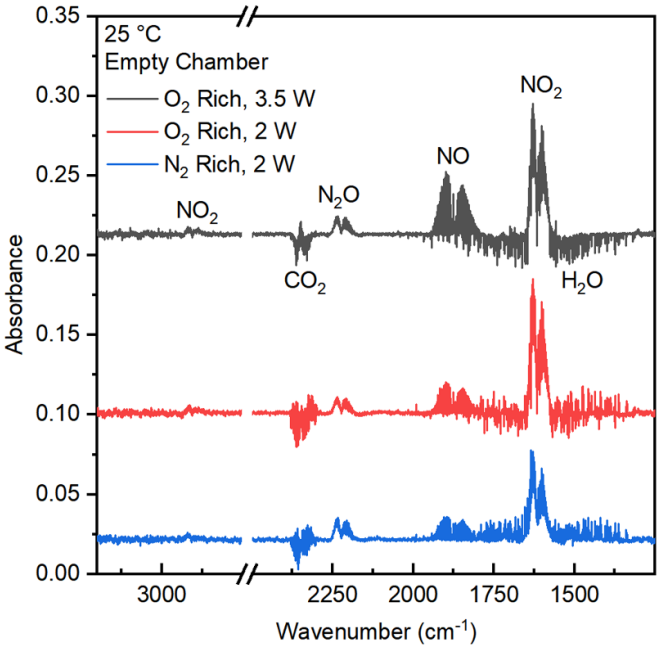

Figure 2. FTIR spectra of downstream gas products from plasma exposure to an empty chamber at 25 °C. Spectral intensity of downstream species varies linearly with concentration. NO_2 and NO increase with O_2:N_2 ratio and plasma power, N_2O varies little. H_2O results in noise from 1200 cm^{-1} to 2000 cm^{-1}.

IR features corresponding to CO_2 and H_2O are also visible in all conditions. CO_2 and H_2O are attributed to trace atmospheric contamination and are not further analyzed in this work. No RONS are seen downstream without plasma for all catalyst temperatures and gas flow conditions evaluated in this work. This is expected as catalyst temperatures employed in this work are too low for thermal NO formation [19]. In this work NO_x is defined as the sum of NO, NO_2, HNO_3, and $2xN_2O_5$. However, NO and NO_2 and N_2O are typically the only species seen downstream.

Initial product quantification focused on yields of species that are formed by the plasma in the gas phase. This was to verify how reactions in the plasma varied with plasma-power and O_2/N_2%. Figure 3 shows the effects of changing the plasma-gas mixture and plasma power on plasma products in an empty chamber. O_2 rich plasma allows for higher deposited power before arcing to the chamber walls, thus the range shown is larger. Additionally, at a higher powder bed temperature, the plasma plume begins to arc at a lower power, likely because of a higher gas temperature within the reaction chamber. When O_2:N_2 ratio is increased, more NO_2 appears downstream, with O_3 beginning to appear below 1 W at 25 °C. When plasma power is increased, NO takes up a larger portion of total product regardless of the jet gas. Total RONS species densities increase almost linearly with increasing plasma power, shown by the NO_x curves. Species other than NO, NO_2

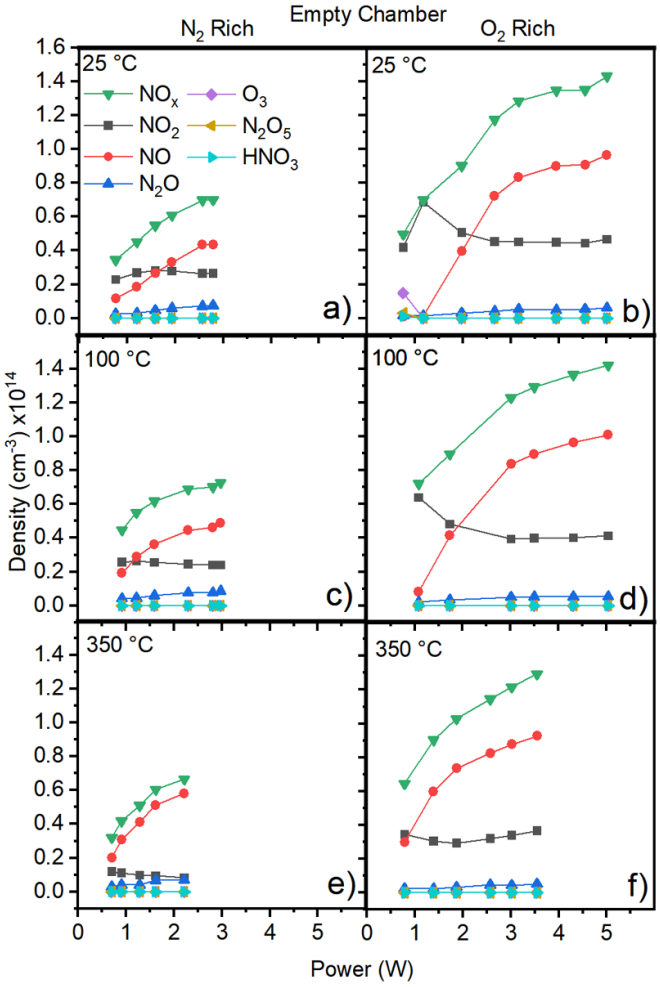

Figure 3. Variation of plasma produced NO_x species with increasing power deposited in the plasma jet with no catalyst present. Exposure time was 15 min. (a) N_2 rich feed gas, 25 °C powder bed. (b) O_2 rich feed gas, 25 °C powder bed. (c) N_2 rich feed gas, 100 °C powder bed. (d) O_2 rich feed gas, 100 °C powder bed. (e) N_2 rich feed gas, 350 °C powder bed. (f) O_2 rich feed gas, 350 °C powder bed.

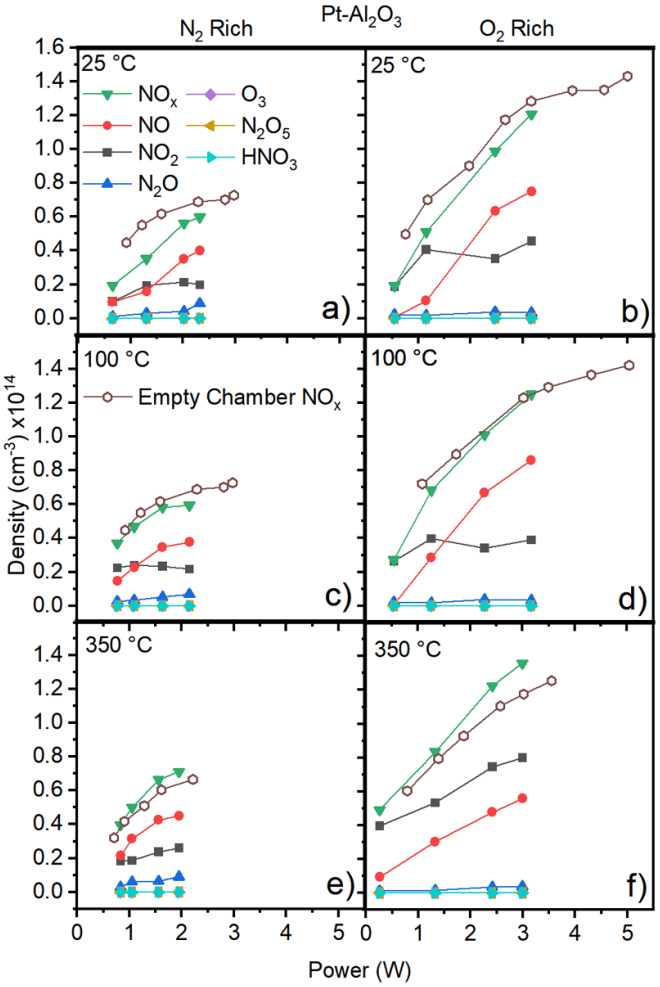

Figure 4. Variation of plasma produced NO_x species with increasing power deposited in the plasma jet over Pt-Al_2O_3. Samples were exposed for 30 min at each power starting at the lowest power and moving to the highest, for 25 °C, then 100 °C, then 350 °C. The N_2 rich and O_2 rich data are taken from a separate powder sample. NO_x from the empty chamber is shown for comparison. (a) N_2 rich feed gas, 25 °C powder bed. (b) O_2 rich feed gas, 25 °C powder bed. (c) N_2 rich feed gas, 100 °C powder bed. (d) O_2 rich feed gas, 100 °C powder bed. (e) N_2 rich feed gas, 350 °C powder bed. (f) O_2 rich feed gas, 350 °C powder bed. For comparison, total NO_x measured for the empty chamber is shown as well.

and N_2O are only seen at very low power for O_2 rich plasma at 25 °C, where small quantities of O_3 and N_2O_5 are measurable. Increasing temperature results in a shift from NO_2 to NO for both gas feeds. Because the products are measured downstream of the reaction chamber, the measured densities may differ from the fluxes impinging on the catalyst surface, even for empty chamber conditions shown in figure 3. This is discussed further in section 4.1.

The effect of variation of plasma power on measured product densities with the Pt-Al_2O_3 catalyst in place is shown in figure 4. A smaller power range is shown for Pt-Al_2O_3 than for the empty chamber in figure 3. The power was restricted with the catalyst present to avoid arcing, which may affect the catalyst in unknown ways and reduce experimental repeatability. Arcing was less of a concern for an empty chamber, as tests could be repeated quickly, with less time and material lost in the event of arcing. Again, increasing O_2:N_2 ratio increases the amount of NO_2 seen downstream. For Pt-Al_2O_3 at low temperature, NO eclipses NO_2 at high plasma power, similar to an empty chamber. At very low power, NO is more prominent for N_2 rich plasma than O_2 rich. After around 1.5 W, O_2 rich plasma is more effective at both NO and NO_2 production at low temperature. At 350 °C, both NO_2 and NO increase with power for N_2 and O_2 rich plasma. This effect is especially prominent for O_2 rich plasma. Total RONS species densities rise linearly with increasing plasma power for all conditions. No species other than NO, NO_2 and N_2O are seen.

To get a better idea of the species that form with a greater O_2 surplus, an O_2/Ar plasma was interacted with an unexcited stream of N_2/O_2/Ar in the empty reaction chamber. Figure 5

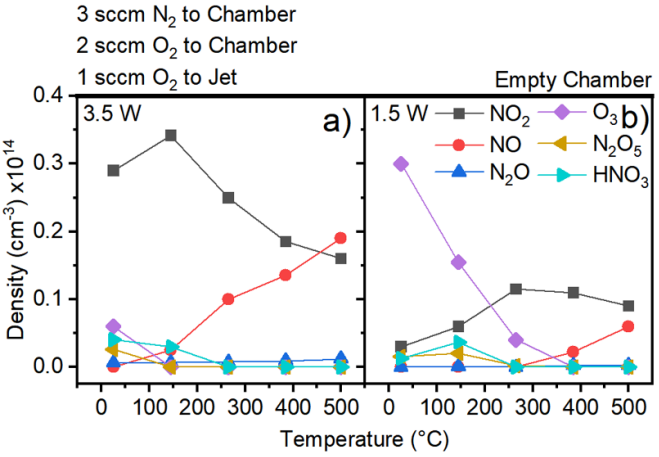

Figure 5. Variation of downstream species with powder bed temperature for an empty chamber. Gas flow conditions here are not consistent with the rest of this work, and include an argon-backed (400 sccm) unexcited gas flown into the reaction chamber along with the plasma gas. The pattern of density variation with temperature is consistent with all $N_2/O_2/Ar$ plasma variations tested. (a) 3.5 W plasma power. (b) 1.5 W plasma power.

shows these results. This gas flow configuration is not used elsewhere in this work. However, it gives a better understanding of how species such as O_3 vary with powder bed temperature. Figure 5(b) shows that, for low-power plasma, O_3 drops rapidly with increasing powder bed temperature. It should be noted that the temperatures displayed in this work are not representative of the gas temperature. The flow rates employed are too high for equilibration with the powder-bed set temperature. While the gas temperature will certainly impact gas phase reactions, especially concerning O_3 [23], the degree of gas heating due to flow through the powder bed was not evaluated in this work.

3.1.2. Plasma–catalyst interaction at constant temperature. The catalyst powder was exposed to plasma at a constant temperature for extended periods of time to understand its interaction with the plasma at steady state. Experiments were performed with both Pt-Al_2O_3 and Al_2O_3 to characterize the role of Pt. Three temperatures were chosen to analyze, 25 °C, 100 °C, and 350 °C. At 25 °C and 100 °C, Pt is not active for NO oxidation with O_2, at 350 °C it is [33].

A comparison of downstream product densities for Pt-Al_2O_3, Al_2O_3, and an empty chamber during exposure to N_2 or O_2 rich plasma is presented in figure 6. Only three downstream species were seen in the FTIR spectra, NO_2, NO, and N_2O. The density of N_2O is much lower than the densities of NO and NO_2 under all conditions. Additionally, N_2O hardly varies with conditions and as such is not analyzed further in this work.

For the empty chamber, the measured density plateaus and becomes stable quickly, within 5 min. However, densities take longer to stabilize with Al_2O_3, with 20 min being typical. Pt-Al_2O_3 requires even more time, 40 min at 350 °C for N_2 rich gas and 50 min at 350 °C for O_2 rich gas. At low temperatures, downstream densities do not appear to have stabilized after even 60 min for Pt-Al_2O_3. This is especially noticeable for O_2 rich plasma.

Downstream densities of NO and NO_2 are consistent for both 25 °C and 100 °C for all conditions and materials. For Al_2O_3 and the empty chamber, 350 °C results in a drop in NO_2 production, with an increase in NO production. This shift is more prominent for N_2 rich plasma. For N_2 rich plasma over Pt-Al_2O_3 at 350 °C, both NO and NO_2 increase relative to low temperatures. For O_2 rich plasma over Pt-Al_2O_3 at 350 °C, NO_2 increases dramatically relative to low temperatures while NO is lessened. In contrast to Al_2O_3 or an empty chamber, NO_2 density with Pt-Al_2O_3 is highest at 350 °C. The downstream product densities with N_2 rich plasma over Pt-Al_2O_3 are the same for all three temperatures for the first 15 min of exposure. After 15 min, densities at 350 °C rise rapidly. This pattern is not as evident with O_2 rich plasma, however a change in the slope of product increase does occur after around 10 min. Figures 6(10) and (11) show that the initial rapid rise in density from plasma-on is similar with both Pt-Al_2O_3 and bare Al_2O_3. After this, the slope remains positive for Pt-Al_2O_3 while Al_2O_3 levels off.

To tabulate the overall enhancement of reactive nitrogen production, the total N in all downstream species was summed for each temperature and material according to equation 3.2 below:

$$N_{tot} = NO_2 + NO + 2 * N_2O. \tag{3.2}$$

This value is shown in figures 6(19)–(24). At 25 °C and 100 °C there is slightly less N_{tot} and O_{tot} after 1 h compared to Al_2O_3 and an empty chamber. At 350 °C there is a minor enhancement of N_{tot} for Pt-Al_2O_3 relative to Al_2O_3, around 10% for N_2 rich plasma and around 20% for O_2 rich plasma.

Total bound oxygen, O_{tot}, was calculated according to equation (3.3) below, and is also shown in figures 6(25)–(30)

$$O_{tot} = 2 * NO_2 + NO + N_2O. \tag{3.3}$$

For O_{tot}, the differences between materials are pronounced. For 350 °C, Pt-Al_2O_3 shows a higher value than Al_2O_3 and an empty chamber. For N_2 rich plasma, Pt-Al_2O_3 at 350 °C and empty chamber at 25 °C have a similar O_{tot} value. For O_2 rich plasma, Pt-Al_2O_3 has a larger O_{tot} value than for all other conditions.

3.1.3. Plasma–catalyst interaction under thermal cycling. Steady state data may not be sufficient for understanding the changes to the catalyst that occur under plasma exposure. Temperature variation is useful for visualizing changes to the catalyst that may affect its performance, such as catalyst activation demonstrated in the work of Li *et al* [13]. Thermal cycling of the catalyst powder under plasma exposure was employed to identify these changes. Thermal cycling may also help determine what the relative contributions of the plasma and the material surface are to the downstream gas products.

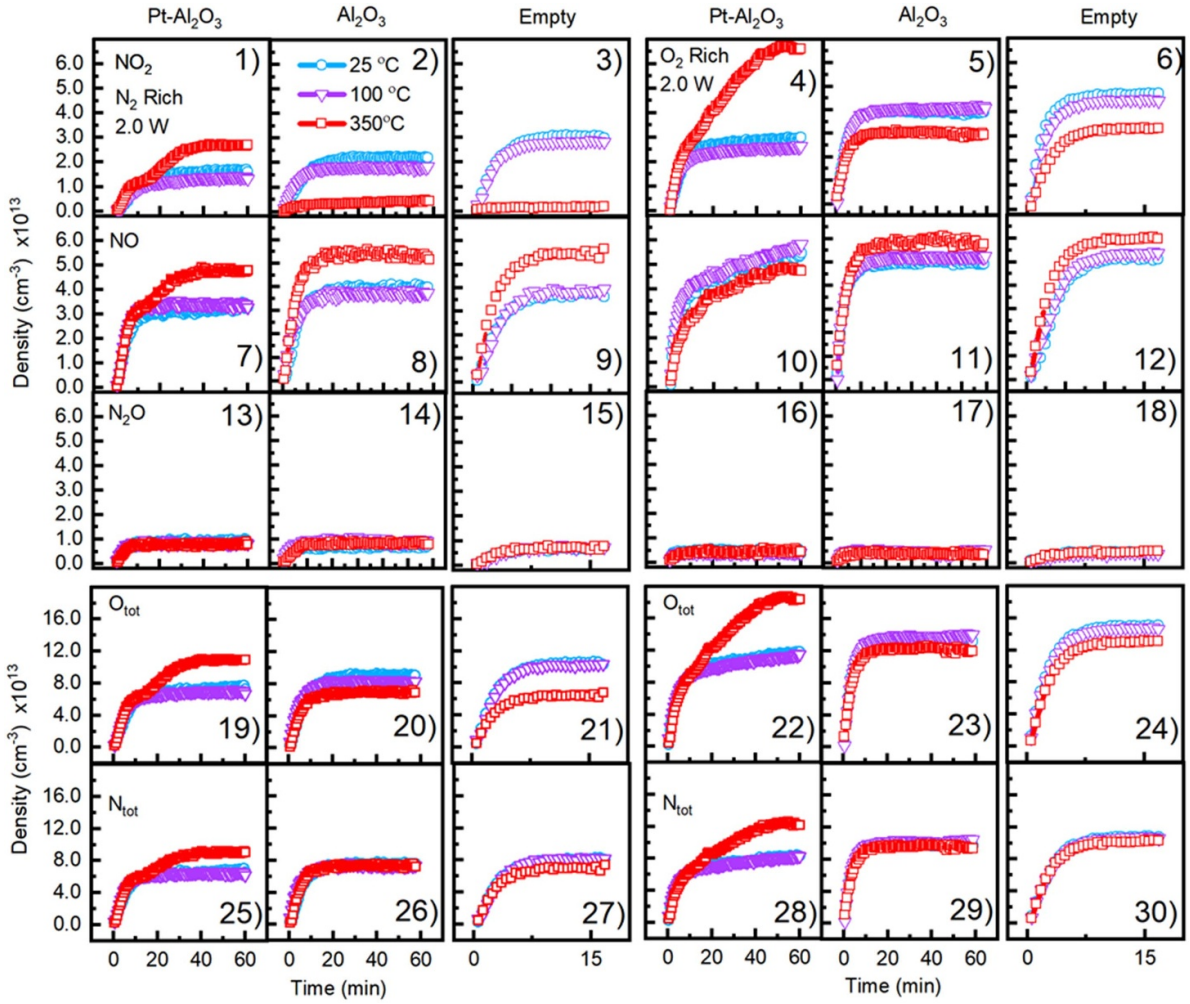

Figure 6. Densities of downstream gas products during long-term plasma exposure to Pt-Al_2O_3, Al_2O_3, or an empty chamber with powder bed temperatures of 25 °C, 100 °C, and 350 °C. 2 W plasma used throughout. Empty chamber only presents 20 min of exposure. (1)–(3) NO_2, N_2 rich. (4)–(6) NO_2, O_2 rich. (7)–(9) NO, N_2 rich. (10)–(12) NO, O_2 rich. (13)–(15) N_2O, N_2 rich. (16)–(18) N_2O, O_2 rich. (19)–(21) O_{tot}, N_2 rich. (22)–(24) O_{tot}, O_2 rich. (25)–(27) N_{tot}, N_2 rich. (28)–(30) N_{tot}, O_2 rich.

The standard pattern for these experiments was to cycle the material, either Pt-Al_2O_3 or Al_2O_3, from 100 °C to 350 °C at a fixed rate, e.g. 10 °C min^{-1}, repeatedly, with no gap between the cycles. 100 °C was chosen because downstream products for 25 °C and 100 °C are roughly equivalent (figure 6) and below 100 °C the cooling system of the reaction chamber cannot cool at 10 °C min^{-1}. Thermal cycling is a technique common in the evaluation of catalytic reactions that has not been widely applied to plasma catalysis [34]. First presented is thermal cycling carried out in an empty chamber to see what interactions may be occurring regardless of catalyst powder. Next, a comparison of thermal cycling with Pt-Al_2O_3 and Al_2O_3 is shown for an understanding of the role of Pt. Finally, thermal cycling of Pt-Al_2O_3 under different plasma conditions is shown, to discern the role of the plasma.

Figure 7 shows downstream densities captured during thermal cycling with no catalyst powder. NO and NO_2 increase and decrease respectively as temperature is raised for both feed gas compositions. The decrease in NO_2 is likely caused by destruction of oxidizers like O_3 on the hot surface of the powder cup or due to gas heating. A slight hysteresis pattern is apparent, particularly for NO_2 density with N_2 rich plasma. The reason for this hysteresis is unknown, but may indicate a surface interaction that changes the state of the catalyst-cup walls. O_2 rich plasma shows an increase of NO and NO_2 relative to N_2 rich plasma for the same power.

Figure 8 shows downstream NO_2 and NO products during thermal cycling under constant exposure to plasma for both Pt-Al_2O_3 and Al_2O_3. Downstream products with Pt-Al_2O_3 strongly show temperature-dependent formation, with NO_2 and NO densities rising rapidly as the temperature is raised to form a hysteresis loop. Four thermal cycles were performed for both feed gas configurations. For Pt-Al_2O_3, the size of this hysteresis loop increases across the first 3 cycles and becomes reproducible after the third. Al_2O_3 on the other hand, has a near identical pattern for all four cycles. The changes taking place during these first three cycles have been analyzed in [35]. However, the present work focuses on conditions where

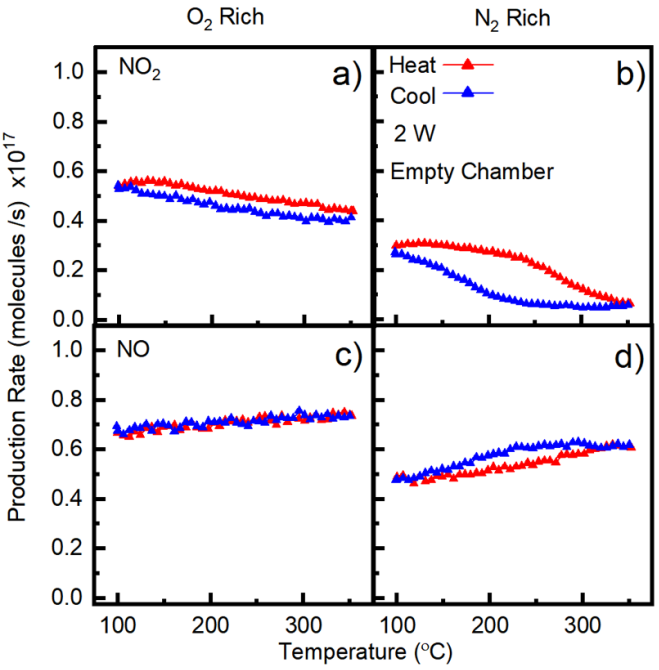

Figure 7. Production rate of downstream products during thermal cycling of an empty powder cup under constant plasma exposure. 2 W plasma. 10 °C min^{-1} as the heating and cooling rate. Cycles were consecutive with no gap in between, and only the third cycle is shown. (a) NO_2 measured with O_2 rich plasma. (b) NO_2 measured with N_2 rich plasma. (c) NO measured with O_2 rich plasma. (d) NO measured with N_2 rich plasma.

the surface has stabilized and thus only the third cycle is analyzed.

For N_2 rich plasma, no sharp NO_x increase occurs for Al_2O_3 during the temperature ramp. A slight shift towards NO is seen at higher temperatures, consistent with figure 6, but there is no obvious change during the temperature ramp. At lower temperatures, twice as much NO and slightly more NO_2 is present downstream with Al_2O_3 than Pt-Al_2O_3. After 280 °C, downstream NO_x for Pt-Al_2O_3 rapidly eclipses that of Al_2O_3, with NO_2 showing the larger difference. O_2 rich plasma over Al_2O_3 shows clear hysteresis, with both NO and NO_2 increasing around 225 °C and peaking around 275 °C. The hysteresis pattern for Al_2O_3 and Pt-Al_2O_3 is not similar, suggesting a different reaction mechanism.

While both gas flow conditions show temperature dependent product formation over Pt-Al_2O_3, the hysteresis loop is more pronounced with O_2 rich conditions. For NO_2, the start of the hysteresis loop occurs at a lower temperature for O_2 rich (∼250 °C) than N_2 rich plasma (∼280 °C). The increase in NO_2 density is also steeper for O_2 rich plasma. NO_2 density peaks at 325 °C for O_2 rich plasma and 350 °C for N_2 rich plasma. NO density also rises at a slightly lower temperature for O_2 rich plasma, with a shallower curve. With increasing O_2:N_2 ratios, downstream NO_x is boosted at all temperatures. This is shown in figures 8(e) and (f), where the rolling sum totals across the full cycle are shown. Total NO_2 production is 3x larger for O_2 rich across the whole cycle, while NO totals are around 30% larger.

Figure 3(d) indicates that increasing plasma power for O_2 rich plasma significantly changes the NO flux to the catalyst surface. To investigate these effects, 2 W and 3.5 W power for O_2 rich plasma was applied to the catalyst during thermal cycling, and results are displayed in figure 9. Densities of both NO and NO_2 have a consistent pattern during catalyst cooling for high and low power. NO_2 heating curves change significantly as the power is raised, with the temperature of product-formation lowering as the power increases. From 2 W to 3.5 W the temperature of NO_2 increase drops around 50 °C. NO_2 downstream density also peaks 50 °C earlier for 3.5 W plasma, 275 °C compared to 325 °C. Low temperature NO_2 does not vary across power, consistent with the empty chamber results in figure 3(d). NO heating curves show a distinct peak at low temperature, in the range of 150 °C. This peak is also seen with 2 W N_2-rich plasma but is more easily visualized in figure 9(b) as it increases with plasma power. NO density also rises at a slightly lower temperature for 3.5 W plasma, with a shallower curve. Total NO and NO_2 produced during the cycle increase by a similar amount for 3.5 W vs 2 W plasma.

To determine the importance of the non-excited component of the gas stream during thermal cycling, namely O_2, Pt-Al_2O_3 was exposed to 3.5 W O_2 rich plasma for three thermal cycles. This was followed by a fourth thermal cycle with the plasma turned off. In the plasma off cycle, O_2 flow was either constant or shut off. The results are shown in figure 10. In both cases there is an initial drop in downstream density due to turning off the plasma (near 100 °C). After this drop a hysteresis pattern is present with a clear temperature dependence of the product formation. The ratio of NO_2 to NO changes when O_2 is extinguished. With no O_2 flow, there is a 100% increase in peak NO and a similar decrease in NO_2, compared to leaving the O_2 flow on. The lower panels of figure 10 show the rolling sum totals for when O_2 is either flowing or cut off. Total NO_x is almost identical for both conditions, suggesting that while the oxidation state of the products changes, the release propensity is not affected by O_2.

Downstream measurements are not sufficient to gain a complete understanding of the surface mechanisms taking place on the catalyst surface. Thus, characterization of surface absorbed species with DRIFTS was carried out as detailed in the next section.

3.2. Analysis of surface species

Real time characterization of IR sensitive species adsorbed on the catalyst or support surface was accomplished with DRIFTS. Examples of DRIFTS spectra are shown in figure 11. Quantitative calculations of surface coverage for DRIFTS peak heights were not attempted in this work. Absorbance peaks were approached qualitatively, with variations in peak height assumed to correspond to changes in surface coverage. Figure 11 shows the surface species present upon heating to high temperature under pure Ar flow with no plasma. Negative peaks present in the region 1000–2000 cm^{-1}, as well as the wide band present 2500–3500 cm^{-1} are attributed to surface water that is removed as the catalyst is heated [8, 22]. These

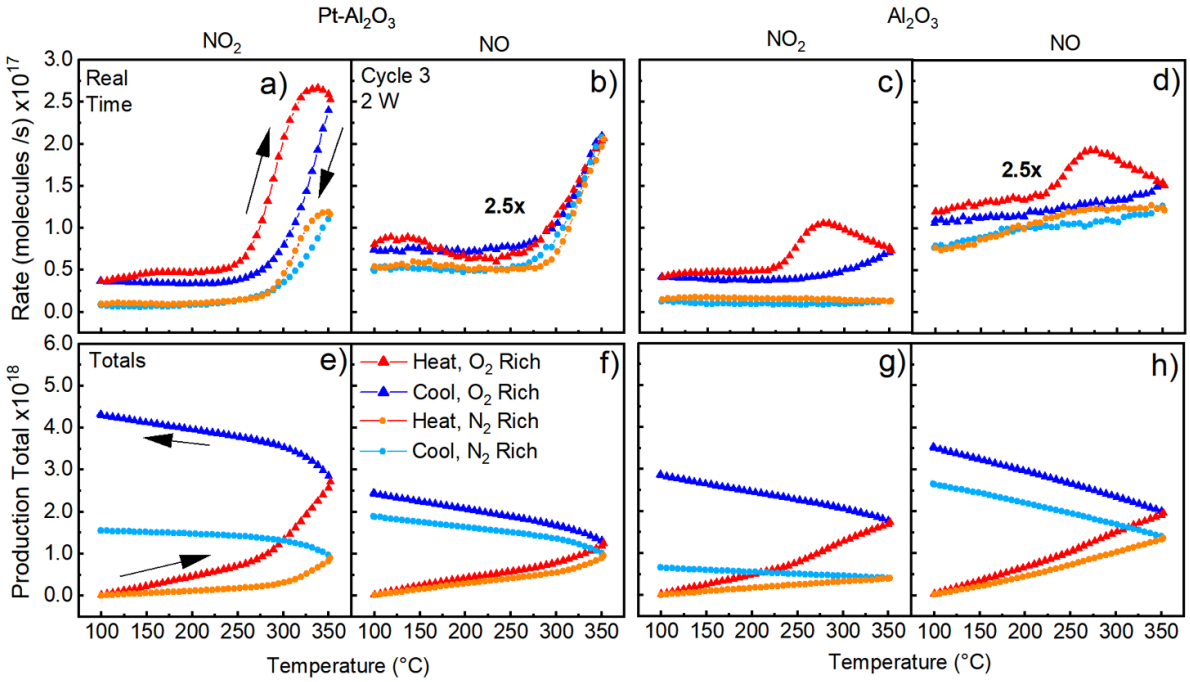

Figure 8. Production rate of downstream products during thermal cycling of Pt-Al_2O_3 or Al_2O_3 under constant plasma exposure. 2 W N_2 rich or O_2 rich plasma was used. 10 °C min^{-1} was used as the heating and cooling rate. Cycles were consecutive with no gap in between. (a) NO_2 production rate, Pt-Al_2O_3. (b) NO production rate, Pt-Al_2O_3, multiplied by 2.5 for greater clarity. (c) NO_2 production rate, Al_2O_3. (d) NO production rate, Al_2O_3, multiplied by 2.5 for greater clarity. (e) Rolling sum NO_2, Pt-Al_2O_3 (f) Rolling sum NO, Pt-Al_2O_3. (g) Rolling sum NO_2, Pt-Al_2O_3 (h) Rolling sum NO, Al_2O_3.

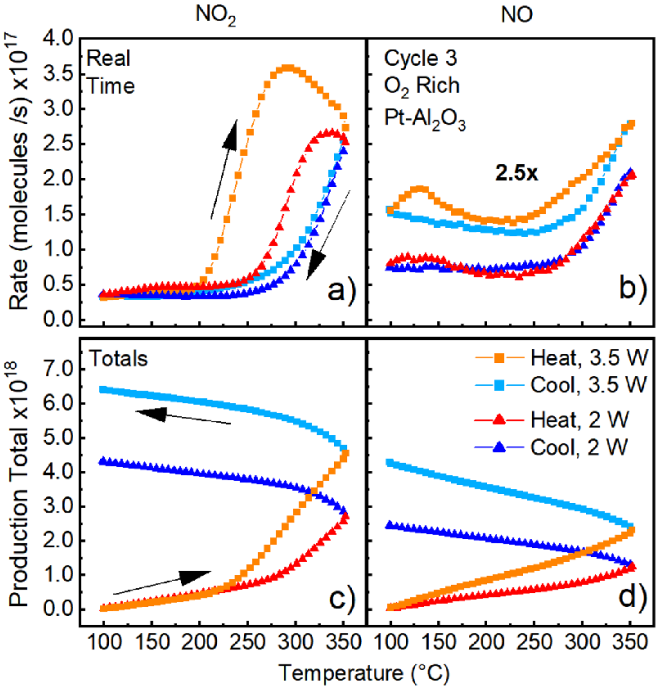

Figure 9. Production rate of downstream products during thermal cycling of Pt-Al_2O_3 under constant O_2 rich plasma exposure at either 2 W or 3.5 W. 10 °C min^{-1} was used as the heating and cooling rate. Cycles were consecutive with no gap in between; the third cycle is shown. (a) NO_2 production rate. (b) NO production rate, multiplied by 2.5 for greater clarity. (c) Rolling sum NO_2. (d) Rolling sum NO.

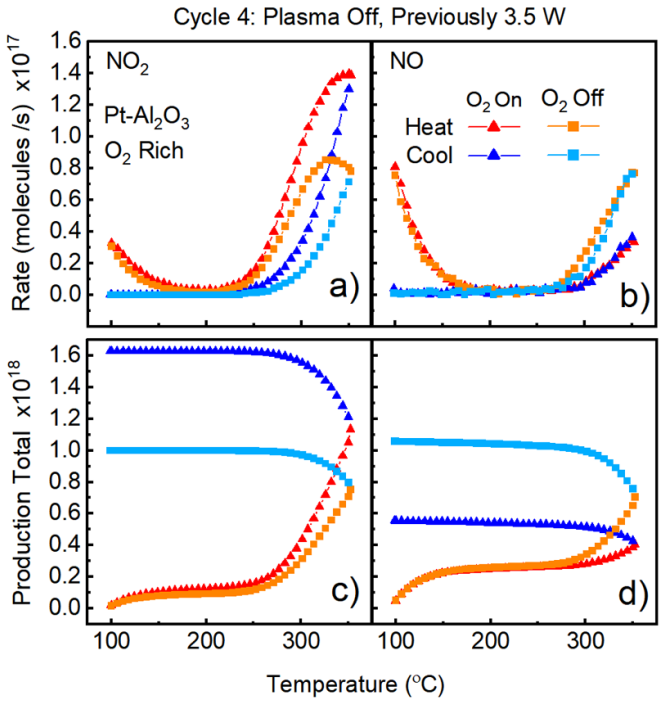

Figure 10. Production rates of NO_x after three thermal cycles of Pt-Al_2O_3 under 3.5 W, O_2-rich plasma exposure (not shown). In the 4th cycle, which occurred directly after the third cycle, plasma was turned off. This situation was also examined in a case where O_2 flow during the 4th cycle was additionally turned off. Results show that the hysteresis pattern of product formation is a surface effect, and that the O_2 availability at elevated catalyst temperature increases the abundance of downstream NO_2 relative to NO. (a) NO_2 production rate. (b) NO production rate. (c) NO_2 rolling sum totals. (d) NO rolling sum totals.

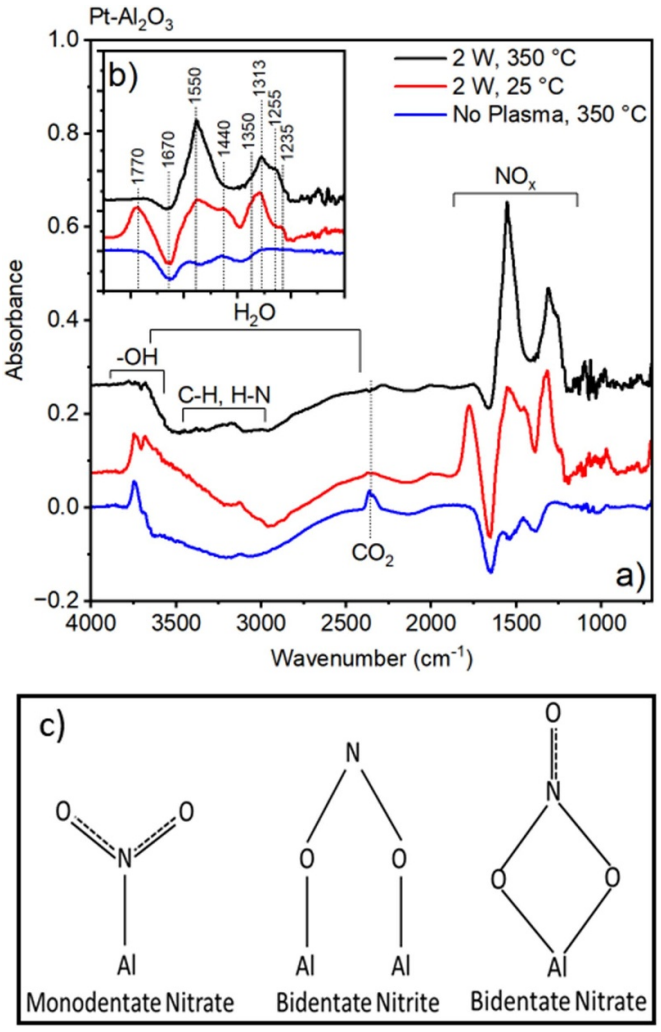

Figure 11.: (a) DRIFTS spectra of Pt-Al_2O_3 catalyst at 350 °C with no plasma (bottom) and pure Ar flow, 25 °C with N_2 rich plasma (middle), and 350 °C with N_2 rich plasma (top). Plasma power was 2 W. The no-plasma spectra was taken after heating to 350 °C with a background spectra at 100 °C. The plasma spectra were captured after 45 min of exposure to fresh catalyst at the referenced temperature, with a background spectrum at the referenced temperature. (b) Spectral region 1000–1900 cm^{-1}, prominent absorbance peaks are highlighted. (c) Chemical structure of observed species.

peaks increase and decrease linearly with temperature. Other features in the region of 3700 cm^{-1} and 3250 cm^{-1} are attributed to hydroxyl groups [36–40] and potentially C–H [41–43] or H–N [41, 44] bonds respectively. These features are quite noisy and are not related to NO_x. Thus, this work will focus on the spectral region of 1000–2000 cm^{-1} where NO_x related peaks appear. With the ignition of plasma, absorbance peaks form in this region. Most peaks correspond to species bonded to the alumina support. Peaks at 1550 cm^{-1} and 1255 cm^{-1}, are attributed to monodentate nitrate (NO_3^-) on alumina [45–54]. 1550 cm^{-1} and 1255 cm^{-1} have the same variation pattern. 1313 cm^{-1} is more difficult to classify. Al_2O_3 based peaks in the range of 1313 cm^{-1} have been attributed to both nitrite and nitrate in the literature [49, 55–57]. Based on the peak stability, nitrate may be more likely, as nitrite is typically reduced at 350 °C [48, 58]. However, the peak is also convoluted with overlaps from 1350 cm^{-1} and 1255 cm^{-1}. Based on [49, 51] this peak is classified as bidentate nitrate in this work. A shoulder at 1235 cm^{-1} can be seen in some conditions, which is attributed to bidentate nitrite [45, 50, 51, 56, 57, 59]. The peak at 1770 cm^{-1} can be attributed to Pt-NO [48, 60] and is not seen for Pt at elevated temperature. Additionally, the peaks at 1440 cm^{-1} and 1350 cm^{-1} are attributed to solvated nitrate, resulting from the interaction of water impurities in the feed gas with nitrate on the alumina surface [49, 51–53, 61]. An overview of the relevant peaks is also shown in table 1.

3.2.1. Surface species evolution at constant temperature. The evolution of surface peaks on Pt-Al_2O_3 and Al_2O_3 under plasma exposure at constant temperature were evaluated to correlate with the downstream data shown in figure 6. Figure 12 shows the primary surface species over time for both Pt-Al_2O_3 and Al_2O_3 under exposure to N_2 rich plasma conditions. The peaks are broadly similar for both materials. The negative peak at 1670 cm^{-1} was assessed to be due to removal of water from the surface as it varies linearly with temperature and appears if the catalyst is heated in pure Ar. The intensity

Table 1. Assignment of vibrational frequencies for adsorbed species on Pt-Al_2O_3 or Al_2O_3 surface.

Vibrational frequency (cm^{-1})	Surface species—Platinum (reference)
1770	NO [46, 58]
	Surface species—Alumina (reference)
1670	H_2O [22]
1550	Monodentate Nitrate [43–46, 48, 60–62]
1313	Bidentate Nitrate [46, 48]
1255	Monodentate Nitrate [43, 44, 48, 58, 60]
1440	Solvated Nitrate [47, 49, 50]
1350	Solvated Nitrate [51, 59]
1235	Bidentate Nitrite [43, 48, 49, 54, 55, 57, 61, 62]

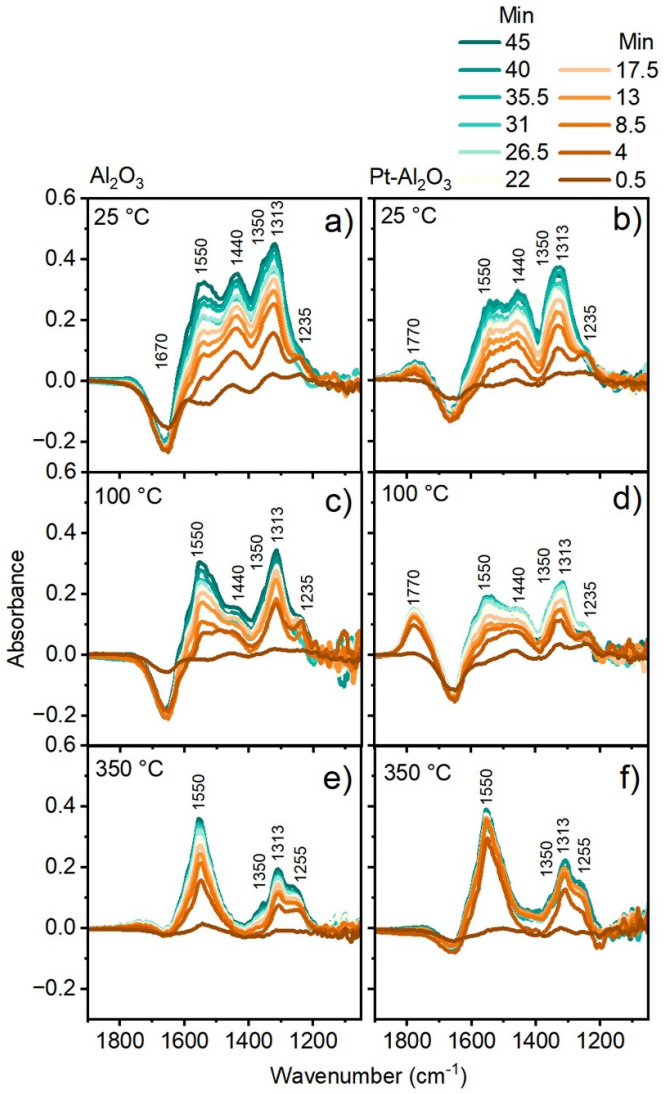

Figure 12. DRIFTS absorbance peak heights after 45 min of 2 W, N_2 rich plasma exposure. Exposures were conducted at 25 °C, 100 °C, and 350 °C. The background spectrum was taken at the temperature of test immediately before plasma exposure. Columns are for different materials, rows for different temperatures. For frequency assignment, see table 1. (a), (b) 25 °C, Pt-Al_2O_3 and Al_2O_3. (c), (d) 100 °C, Pt-Al_2O_3 and Al_2O_3. (e), (f) 350 °C, Pt-Al_2O_3 and Al_2O_3.

of this peak depends on the initial background spectra. For 350 °C exposure, the background was taken at 350 °C and thus most water was already removed from the surface. For Al_2O_3, no peak is seen at 1770 cm^{-1}, supporting the interpretation of that peak as Pt-NO. Nitrate species on Pt-Al_2O_3 at 350 °C (figure 12(f)) increase faster than for all other conditions. The nitrite shoulder at 1235 cm^{-1} is initially present at low temperatures before being subsumed by nitrates at 1313 cm^{-1} or 1255 cm^{-1}. Solvated nitrate decreased with temperature, consistent with the elimination of water. The most prominent trend across temperature is the decrease of water solvated nitrate. Monodentate nitrate appears to increase in expense of solvated nitrate.

Pt-NO builds up rapidly on the Pt surface at 100 °C, while nitrate peaks are lower than for Al_2O_3 for the same temperature. This suggests that some NO_x storage is in the form of Pt-NO at these temperatures.

It must be emphasized that each curve in both figures 6 and 12 represents a fresh sample and exposure. Exposing a sample at 100 °C and then shifting to 350 °C does not necessarily result in comparable peak-height shifts. This is further explored when discussing thermal cycling of catalyst samples under plasma exposure.

3.2.2. Surface species evolution during thermal cycling. Surface analysis during thermal cycling was employed to understand what surface processes take place during the prominent hysteresis visible in the downstream product measurements. Figure 13 shows surface species evolution during the third thermal cycling of Pt-Al_2O_3 or Al_2O_3 under 2 W N_2-rich plasma. The overall surface species are the same for both materials, with the exception of Pt-NO. The most prominent pattern for both materials is the solvated nitrate—monodentate nitrate shift that takes place with changing temperature. This is presumably due to water leaving the surface. Al_2O_3 seems to show a greater response of solvated nitrate to temperature, suggesting weaker water attachment. Aside from a shift between water solvated and monodentate nitrate, peaks related to the support do not show any drastic changes with temperature. Pt-NO on the other hand, begins a steep decrease when heated to 175 °C and levels off at around 250 °C. A hysteresis pattern is

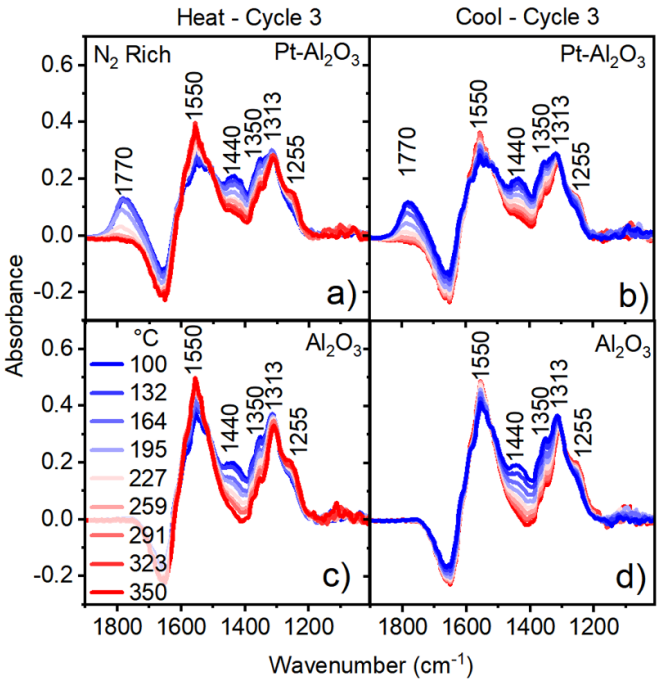

Figure 13. DRIFTS absorbance peaks during the third thermal cycle of Pt-Al_2O_3 or Al_2O_3 under plasma exposure to 2 W N_2-rich plasma. Background spectra were taken at 100 °C before the start of plasma exposure/cycling. For frequency assignment, see table 1. (a) Pt-Al_2O_3 heating. (b) Pt-Al_2O_3 cooling. (c) Al_2O_3 heating. (d) Al_2O_3 cooling.

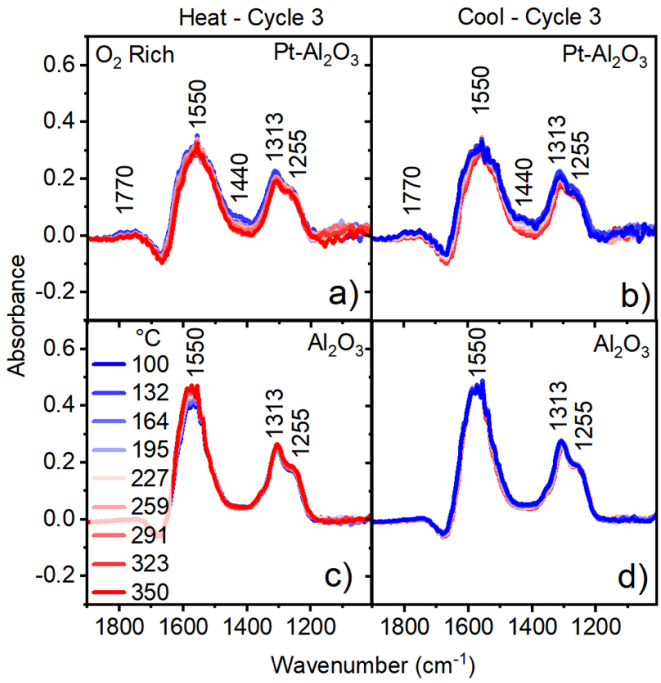

Figure 14. DRIFTS absorbance peaks during the third thermal cycle of Pt-Al_2O_3 or Al_2O_3 under plasma exposure to 2 W O_2-rich plasma. Background spectra were taken at 100 °C before the start of plasma exposure/cycling. For frequency assignment, see table 1. (a) Pt-Al_2O_3 heating. (b) Pt-Al_2O_3 cooling. (c) Al_2O_3 heating. (d) Al_2O_3 cooling.

evident with Pt-NO, with the peak increasing at a slower rate during catalyst cooling.

Figure 14 shows the third cycle for O_2 rich plasma. Solvated nitrate is less prominent for O_2 rich plasma than N_2 rich plasma. This suggests that O_2 rich plasma is more effective at water removal, or that oxidation may prevent the adsorption of water. Al_2O_3 hardly shows water-solvated nitrates at all. A slight Pt-NO peak is apparent with O_2 rich plasma, but it is greatly diminished compared to the N_2 rich case. No clear indication of NO_x release is apparent in the surface species. A small decrease in all nitrate peaks appears to be taking place during heating for Pt-Al_2O_3. While this decrease is repeatable, occurring in cycles 2–4, its magnitude makes attribution to any surface process difficult. Besides this and a decrease in solvated nitrate, the spectra for Al_2O_3 and Pt-Al_2O_3 are quite similar, despite the drastic differences in downstream gas results.

4. Discussion

4.1. Species flux to the catalyst surface

Before discussing the plasma catalyst interaction in full, it is useful to obtain an accurate picture of the incoming species flux arriving at the surface. Our measurement apparatus in this work only permits the quantification of species far downstream of the plasma source. However, significant research on plasma species production in similar jets has been conducted and will be drawn upon to inform the discussion herein.

Prior work with the same APPJ has shown that NO is the primary RONS species which forms in the plasma generation zone (the space between the needle tip and the ring electrode), from the reaction of O and N_2 or N and O_2 [62]. This reaction occurs at short timescales, within the region near the needle tip and the electrode [62, 63]. The primary loss mechanism of NO in the plume and effluent (the regions of the plasma plume extending past the nozzle) is the formation of NO_2, with back reaction of N and NO to N_2 and O also being prominent close to the jet or at high ratios of N_2:O_2 [62, 64, 65]. Atomic O is at its largest concentration near the plasma nozzle, where plasma power dissipation is highest [25, 62, 63]. As the gas moves away from the nozzle, O is quenched through the formation of NO, NO_2, and O_3 [62]. O_3 densities increase past the end of the plasma plume, as other ROS species diminish. Once O is depleted, oxidation of NO is caused by O_3 [65]. For more information, readers are referred to the work of Gaens *et al* and Schmidt-Bleker *et al* [62, 65].

In the setup used in this work, the gas flow exiting the nozzle is 200 sccm, and gas must travel 5 mm to reach the top of the 6 mm diameter powder bed. Based on these values, the estimated travel time of a reactive species between formation and impingement is around 40 ms. Given the short lifetimes of O and N it is unlikely for significant amounts of either one to reach the catalyst surface. The same is true for electronically and vibrationally excited species. Thus, for the

conditions employed in this work, we assume that the primary species impinging on the catalyst surface for both N_2 and O_2 rich conditions are NO and O_3, with some NO_2.

The fact that no O_3 is seen downstream is likely the result of its destruction by NO_x at longer timescales [66], forming NO_2 and N_2O_5 [65]. Figure 5 supports this conclusion, as O_3 and N_2O_5 decrease as the temperature of the powder cup increases, while NO_2 and then NO rise. This decrease is likely due to destruction of O_3 with elevated powder cup temperature and suggests that O_3 destruction by NO_x is significant when NO density from the plasma is high. It also suggests that this destruction likely occurs in the vicinity of or after the catalyst bed. O_3 destruction may take place both on surfaces and in the gas phase. Figure 6 shows the same shift away from NO_2 with temperature for both empty chamber and when the powder bed is filled with Al_2O_3. If a surface was required for O_3 decomposition, one would expect this shift to be more significant for a full powder bed.

Figure 3 shows that NO flux increases with both power and O_2 ratio in the jet. O_3 likely also increases with O_2 admixture to a plasma jet, as higher densities of O_2 in the plasma gas mixture increases the rate of production of O radicals and vibrationally excited O_2 species [13, 62]. Prior work from this group has shown O_3 increase with plasma power for O_2/Ar plasma at the same flow rates and time scales, however the increase is not linear [8]. O_3 has also been shown to increase slightly with plasma power for an Ar plasma flown into humid air [64]. In our case, H_2O impurities are not thought to greatly affect NO_x generation within the plasma. Figures 13 and 14 show that the feature due to H_2O at 1670 cm^{-1} does not show a major shift across heating and cooling during cycle 3, suggesting that little water is reintroduced to the surface from impurities in the feed gas. Additionally, the consistency of downstream gas measurements across hours of experimental time suggests that any H_2O impurities in the feed gas are invariant with time.

4.2. Contribution of plasma and catalyst at constant catalyst temperature

Figure 6 shows that catalyst temperature has a large effect on the gas species measured downstream of the plasma catalyst interaction for both Pt-Al_2O_3 and Al_2O_3. Only N_2O shows minimal variation with powder bed temperature or catalyst material, likely because N_2O does not readily adsorb onto Pt, thus all N_2O is formed in the gas phase and merely passes through the catalyst powder [67]. NO_2 shows the most pronounced change with temperature for both O_2 rich and N_2 rich conditions. At 25 °C and 100 °C, Pt-Al_2O_3 results in less NO_2 downstream compared to Al_2O_3 or an empty chamber. This may be due to 60 min not being long enough to reach steady state surface coverage or from dissociation on the catalyst surface, which will be touched on again in section 4.3.2. At 350 °C, NO_2 decreases for Al_2O_3 or an empty chamber due to O_3 destruction. This decrease is smaller for O_2 rich plasma, likely due to a surplus of oxidizing species in the gas phase. For N_2 rich plasma, it is unexpected that NO increases over Pt-Al_2O_3 at 350 °C, as elevated NO_2 suggests that NO is being oxidized. This may be due to changes on the catalyst surface, as densities at 350 °C initially track with low temperature before a divot which occurs at 15 min. This will be explored in section 4.3.2. The initial rise in downstream density does not vary significantly between Pt-Al_2O_3 and Al_2O_3. This may partially be due to the residence time of the gas cell, as the rise in downstream density for an empty chamber is not instant. Figures 6(10) and (11) show how the slopes of NO increase diverge significantly for the two materials after the initial rise. The difference in adsorption characteristics between the materials only affects a fraction of the produced reactive species and is thus best observed over long time scales.

NO_2 production increases over Pt-Al_2O_3 at 350 °C. This can be seen in figures 6(19)–(24), with total captured oxygen increasing by around 50% for Pt-Al_2O_3 relative to Al_2O_3 for N_2 rich and O_2 rich plasma. Figure 4 clearly shows the oxidative ability of platinum. The oxidation effect completely changes how the downstream NO:NO_2 ratio varies with power. At 350 °C, NO_2 and NO both increase with power, whereas for low temperature NO_2 plateaus. When Pt is active for NO oxidation, Pt-O can form from the interaction with O_2 or plasma produced ROS like O_3. This may compensate for the high temperature destruction of gas phase oxidizers like O_3, allowing NO_2 to rise with plasma power. When Pt is not active for oxidation, NO varies with power much like an empty chamber.

Oxidation of NO over Pt with dissociated O_2 is a well-known phenomenon in the temperature range of 150 °C–350 °C [33, 47, 68]. Both the Langmuir–Hinshelwood and Eley–Rideal mechanism can take place [33, 68, 69]. Interestingly, with N_2 rich plasma, the oxidation capability of low temperature plasma in an empty chamber is similar to that of high temperature Pt-Al_2O_3. This suggests that O_3 in the gas phase is a potent oxidizer in the gas phase. However, when O_2:N_2 ratio is increased this is no longer true and surface oxidation becomes dominant. The oxidation capability of Pt can also be seen in the DRIFTS data, where nitrate peaks increase rapidly for Pt-Al_2O_3 at 350 °C under N_2 rich plasma exposure (figure 12(f)). Pt is known to catalyze nitrate formation on Al_2O_3 based NO_x adsorbers [58]. Nitrates were the primary surface species to build up in during plasma exposure although there appeared to be the presence of a nitrite shoulder initially at low temperatures. Nitrite formation is known to proceed nitrate formation on Pt-Al_2O_3 [58, 70, 71], however at high temperatures this may occur too quickly to resolve.

Total captured nitrogen (figures 6(25)–(30)) also shows a small increase for Pt-Al_2O_3 relative to Al_2O_3 or an empty chamber at 350 °C. This can also be seen in the NO_x curves from figure 4. It is not clear what causes this increase. It is unlikely that the catalyst enhances oxidation of nitrogen through surface reactions, as all excited nitrogen species would be quenched at these time scales [62]. Additionally, the temperature is too low to cause nitrogen dissociation on the surface [19]. It may be that Pt allows for oxidation from NO into more stable species.

Based on this analysis the contribution of the plasma at steady state is as a provider of reactant species to the catalyst surface, particularly NO and oxygen. The catalyst allows for the oxidation by O_2 and O_3 at high temperatures where without catalyst they would not be active.

4.3. Contribution of plasma and catalyst during thermal cycling

Thermal cycling of the catalyst under plasma exposure, as shown in figures 8–10, further clarifies the temperature dependence of the reactions on the catalyst surface. It also allows the separation of transient and long-lasting changes that take place on the catalyst surface.

4.3.1. Transient changes to the catalyst. In the first cycle of plasma exposure, the amount of NO_x formed downstream at high temperatures is low, almost none for N_2 rich conditions. In subsequent cycles, NO_x density at high temperatures increases and the hysteresis loops become stable and reproducible. This effect must be due to long-lasting surfaces changes taking place on the catalyst and is analyzed in [35]. For the purposes of this work, only cycles where the hysteresis pattern becomes reproducible are analyzed. It is immediately clear that this reproducible NO_x hysteresis is due to transient effects, with NO_x being stored at low temperatures and released as the temperature is raised. There is no sign of the type of catalyst activation seen in the work of Li *et al* [13]. When the catalyst is cooled in each cycle, the downstream densities drop to the same level.

Some desorption is apparent from the hysteresis seen for Al_2O_3 under plasma exposure (figure 8). The hysteresis pattern is completely different from that of Pt-Al_2O_3, being complete by 350 °C. Only NO hysteresis is present for Al_2O_3 under N_2 rich plasma exposure, and both NO and NO_2 appear to have an identical release pattern for Al_2O_3 under O_2 rich plasma. This suggests that NO_2 formation is connected with the release of NO. Pt clearly catalyzes this release and catalyzes NO oxidation to NO_2, delaying the appearance of NO downstream. Platinum must then be essential to the storage of NO_x and oxygen at low temperatures and its subsequent reaction/release at high temperatures. L Castoldi *et al* have shown that Pt can catalyze the release of NO_x on Al_2O_3 based adsorbers, so this result is not surprising [58, 72].

The nature of the storage and release changes with plasma composition, and therefore species flux to the surface. Figures 8(a) and 9(a) show that the hysteresis loop of NO_2 increases in size with increasing O_2:N_2 ratio and plasma power. NO, O_2, and likely O_3 flux to the surface is higher for these conditions. Thus, the amount of NO and oxygen adsorption at low temperatures influences the amount of NO and NO_2 formed at high temperatures. Oxidizers are particularly important for NO_2 hysteresis, as figure 8(b) shows that NO is similar between N_2 rich and O_2 rich plasma. Oxygen bound to Pt must be the primary contributor to the increased hysteresis of NO_2, or else O_2 rich plasma would show large NO hysteresis.

Figure 9(a) shows that at 280 °C, the NO_2 density starts to decrease for 3.5 W O_2 rich plasma. This is likely due to a depletion of both NO and Pt-O. Figure 10 shows how released species change when O_2 flow is cut off, with a shift away from NO_2 towards NO. This suggests that Pt-O is depleted first and with no continued oxygen source, NO is released without oxidizing. The initial oxidation is likely covered by Pt-O deposited at low temperatures, from oxidizing species in the plasma. Unfortunately, Pt-O is not directly DRIFTS visible, so oxidation state cannot be confirmed from the data presented here.

Figure 8 also shows that temperature of product formation increase is lowered with O_2 rich compared to N_2 rich plasma at the same power, suggesting a dependence on surface coverage of RONS or oxygen. A larger release of NO_x for conditions with higher flux of reactants to the surface is understandable, as reactant surface coverage is higher. The exact mechanism by which surface coverage changes the start of the hysteresis loop is unclear and requires more investigation.

The primary pattern seen in DRIFTS during thermal cycling (figures 13 and 14) is a repeatable shift from solvated to monodentate nitrate. It is unclear why the peak at 1313 cm^{-1} ascribed here as bidentate nitrate, does not participate in this shift. This pattern does not correlate with any aspect of the downstream gas results.

Storage and release of NO_x on trap catalysts such as Pt-Al_2O_3 or Pt-Ba-Al_2O_3 has been widely studied. NO_x storage is typically attributed to formation of nitrites and nitrates [45, 48, 58, 68, 73, 74]. NO_x release is attributed to NO formed from nitrite and nitrate decomposition, at low and high temperatures respectively [48, 58, 72, 73]. Nitrate decomposition takes place from 300 °C to 500 °C and so would only be beginning in our temperature range [48, 58, 73]. For O_2 rich 2 W plasma, nitrate peaks do appear to decrease slightly at the end of the temperature ramp. However, this is unlikely to be a major contributor to the downstream hysteresis seen. Pt-NO shows the strongest correlation with downstream hysteresis, with a sharp decrease during heating followed by a slower rise during cooling. The Pt-NO decrease temperature occurs before the downstream spike, and appears to be consistent with NO oxidation which typically begins at 150 °C over Pt-Al_2O_3 [33, 75, 76]. The heating curves for downstream NO show a small peak at around 150 °C for both O_2 and N_2 rich conditions (figure 9). This peak correlates well with the initial peak during nitrite TPD in the work of Castoldi *et al* [58]. DRIFTS data does not appear to show the presence of nitrites during thermal cycling at conditions tested here.

Examples from the literature of NO adsorbed on reduced Pt-Al_2O_3 indicate that NO desorption in the 200 °C–300 °C range could be due to Pt-NO bonds [77] and that Pt-NO may make a significant contribution to NO_x storage on reduced Pt-Al_2O_3 [48]. However, in our results, highly oxidizing conditions show the most NO_x storage, and Pt-NO is hardly evident on the surface for 2 W O_2 rich plasma, shown in figure 14. The lack of a clear correlation suggests that there is a species gradient within the catalyst bed. Further investigation is necessary to accurately make an assignment. What

is clear is that at a certain catalyst temperature, a significant amount of NO becomes available for reaction on the catalyst surface.

Based on this analysis, the separate contributions of plasma and catalyst during thermal cycling are described. During thermal cycling, the plasma contributes reactant species at low temperature, both NO and oxidizers such as O_3. The catalyst is able to store these reactants through platinum oxidation and NO storage, making them available for subsequent reaction at high temperatures in a way that would not be possible with plasma alone.

4.3.2. NO adsorption and destruction on the catalyst surface. As shown in figure 8, at lower temperatures, more NO and NO_2 is present downstream with Al_2O_3 than Pt-Al_2O_3. Based on the hysteresis profile, NO_x seems to be absorbed in greater quantities on Pt-Al_2O_3 at low temperatures than on Al_2O_3. However, destruction of NO may also be occurring, and may contribute to differences seen between materials under plasma exposure at constant temperature or during thermal cycling.

To get a better idea of the contribution of adsorption or destruction to suppressed downstream NO_x at low temperature, the total NO_x produced across four cycles was compared to the extrapolated steady-state total at 350 °C for the same length of time. These results are shown in figure 15. The steady-state totals were taken from figure 6. Theoretically, if all the NO_x arriving at the surface is released, the cyclical and steady state totals should be the same at the high point of each cycle. Discrepancies between the two curves could be due to NO destruction or storage of NO_x that is never released. Figure 15 shows that for Al_2O_3, a similar amount of NO_x is formed at steady state and across multiple thermal cycles, 1.54×10^{19} and 1.46×10^{19} respectively for N_2 rich plasma and 2.36×10^{19} and 2.37×10^{19} respectively for O_2 rich plasma. The cyclic curve is also mostly straight, meaning little repeatable absorption and release. It seems that beyond what may be destroyed in both cases, Al_2O_3 seems to store little, despite DRIFTS results in figures 12–14 showing nitrate build up on the surface. This may suggest a gradient of NO_x adsorption within the powder bed for Al_2O_3.

The difference between steady state totals at 350 °C over Pt-Al_2O_3 or Al_2O_3 suggests greater destruction over Al_2O_3. Steady state totals for N_2 rich and O_2 rich plasma over Pt-Al_2O_3 are 1.72×10^{19} and 2.79×10^{19} respectively. This suggests an instability in the plasma produced NO_x for the timescales studied here, which Pt at high temperatures may compensate for. It may be that Pt is able to catalyze the oxidation of NO that would otherwise be destroyed.

The cyclical curves for N_2 and O_2 rich plasma over Pt-Al_2O_3 show a repeated oscillation after cycle 2, indicative of an adsorption and release of NO_x. Figure 15(a) shows that N_2 rich cyclical and steady-state totals grow further apart over time, with the final total of 1.1×10^{19} and 1.72×10^{19}

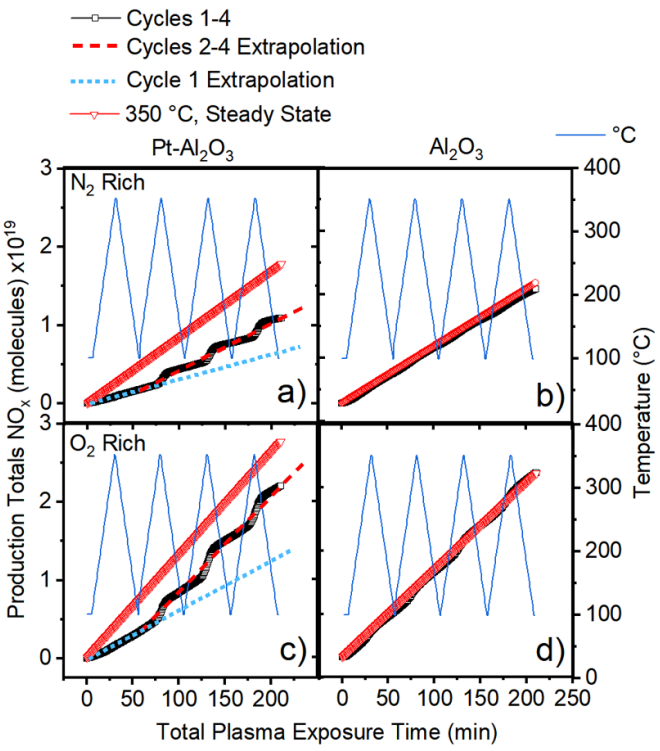

Figure 15. Downstream rolling sum totals of NO_x for all four thermal cycles under plasma exposure compared to steady state exposure for the same length of time. 2 W plasma. Temperature over time is plotted. (a) Pt-Al_2O_3, N_2 rich plasma. An extrapolation of cycle 1 and cycles 2–4 is shown. (b) Al_2O_3, N_2 rich plasma. (c) Pt-Al_2O_3, O_2 rich plasma. An extrapolation of cycle 1 and cycles 2–4 is shown. (d) Al_2O_3, O_2 rich plasma.

respectively. This may suggest a continued destruction of NO at low temperature. By the time the third cycle is reached, downstream hysteresis patterns, and the amount of NO_x formed at high temperature, become repeatable. If steady state and cyclic data continue to grow apart at this point, overall NO loss may be due to destruction rather than adsorption. For O_2 rich plasma (figure 15(c)) after the first two cycles, cyclic and steady state totals increase at similar overall rates, shown by the dashed red line. This suggests a cease of change in permanent storage, and possibly NO destruction if any was occurring.

The main difference between the Pt-Al_2O_3 surface at O_2 rich and N_2 rich conditions is the presence of Pt-NO in DRIFTS for N_2 rich plasma (figure 13). This Pt-NO peak is greatly diminished at low temperature with O_2 rich plasma, suggesting that NO is outcompeted by oxygen for adsorption sites on Pt, and that Pt is mostly oxidized. Metallic Pt may contribute to NO destruction at low temperatures. This could explain why the extrapolation of cycles 2–4 for N_2 rich plasma over Pt-Al_2O_3 has a lower slope than corresponding Al_2O_3 totals, which is not true for O_2 rich plasma. It appears that this destruction is a slower process than oxidation at high temperatures, which results in a higher steady-state total for N_2 rich plasma at 350 °C.

4.4. Summary of plasma–catalyst interaction

From section 4.1 it is determined that the critical flux to the surface consists of NO, O_3, and O_2. All three increase with increasing O_2:N_2 ratio in the feed gas while increased power primarily boosts NO and potentially O_3 as well. At low temperatures, near 100 °C, Pt-O is built up from dissociative adsorption of O_2 as well as oxidation via O_3 and NO_2 which are potent oxidizers [33, 78, 79]. The influence of O_3 and NO_2 means that surface coverage of Pt-O is expected to increase with O_2:N_2 ratio and plasma power. NO_x is absorbed on the surface potentially as Pt-NO or aluminum nitrites and nitrates, it may also be destroyed. The amount of destruction appears to increase with the presence of metallic Pt at low temperatures. However, more investigations are required for this topic.

As the temperature increases, the catalyst becomes active for oxidation of NO. Soon after, depending on the conditions, a large amount of NO is activated on the surface resulting in the start of the hysteresis loops. This NO is oxidized to NO_2 on Pt leading to a NO_2 increase downstream. An increase in downstream NO follows both because NO flux to the surface is no longer stored and because Pt-O is depleted. With Pt-O depleted, incoming oxygen cannot replenish it fast enough to maintain full oxidation.

The transient changes in downstream NO and NO_2 from stored species overlap with a separate increase from the system changing its steady state production values of NO_x. Near the highest temperature of the heating cycle, stored reactants on the surface have been depleted, and steady-state oxidation of the incident NO and oxygen fluxes takes place. As the surface cools, it becomes less active for NO oxidation or desorption, leading to a buildup of NO_x and oxygen on the catalyst surface. There is no point during cooling where NO_2 increases. The overlap at elevated temperature between reactant adsorption and NO oxidation activity must be very small for the conditions tested here.

Thus, there are two mechanisms for NO oxidation demonstrated in this system for the Pt-catalyst. The first is stable, caused by NO and O_2 arriving at the surface at high temperature, and results in the steady state values shown in figure 6. This process dominates the initial part of the cooling cycle. The second is transient and results from reactants stored at low temperatures subsequently reacting at high temperatures to form NO_2 and which leaves the surface. Low temperature Pt-O coverage is critical for this second oxidation pathway meaning that plasma ROS flux to the surface has greater influence.

The different pathways of NO_2 formation can be visualized by plotting NO vs NO_2 production as shown in figure 16. As conditions are changed such that total O_2 and O_3 flux to the surface increases at lower temperatures (increased power, O_2:N_2 ratio) NO_2 and NO production during heating becomes further decoupled. The closer the slope is to one, the lower the oxidation rate, indicating a dearth of surface oxygen and a dependence on incoming O_2 and O_3 for NO oxidation. A high positive slope indicates a significant surplus of surface oxygen compared to surface NO_x. As the Pt-O is depleted, the slope decreases, even turning negative for O_2 rich plasma at 3.5 W. If the surface was only depleted of NO_x the slope would remain vertical. This indicates that depletion of Pt-O at high temperatures is faster than its formation, even with O_2 rich plasma. Once the cooling begins, the slope approaches 1, indicating that NO oxidation is now dependent on incoming O_2 and ROS species. NO_2 hysteresis loops get larger for increasing plasma power and O_2:N_2 ratio in the plasma feed gas. This increase is in large part due to Pt-O, which allows for the rapid oxidation of NO until its depletion.

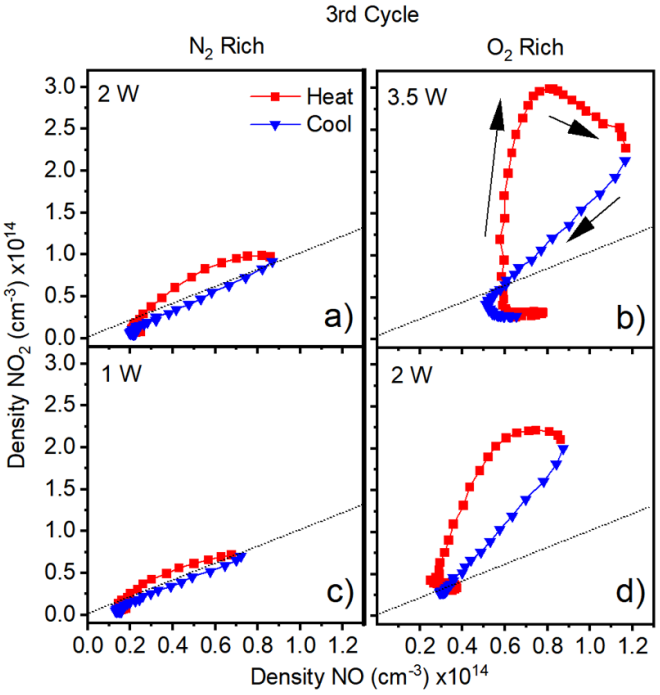

Figure 16. Comparison of NO_2 vs NO production during thermal cycling at different powers and jet gas compositions. NO_2 and NO become further decoupled as the power and O_2:N_2 ratio increases. Arrows indicate the thermal cycle path. (a) 2 W, N_2 rich plasma. (b) 3.5 W, O_2 rich plasma. (c) 1 W, N_2 rich plasma. (d) 2 W, O_2 rich plasma.

Figure 17 illustrates what is believed to be occurring during thermal cycling, based on the results presented in this work. For the sake of simplicity, in this example NO_x is assumed to be stored on the Pt surface as Pt-NO. The primary contribution of the plasma is as an NO and O_3 source that is forced to penetrate the catalyst material. The processes that determine the exact composition of downstream products depend on the nature of the surface with which NO, O_3, and O_2 react. The temperature dependence of product formation and degree of NO oxidation is the result of two overlapping oxidation pathways, one for stored reactants, and the other for reactants arriving at high temperature. For certain conditions, NO may also be destroyed on the catalyst surface at low temperature.

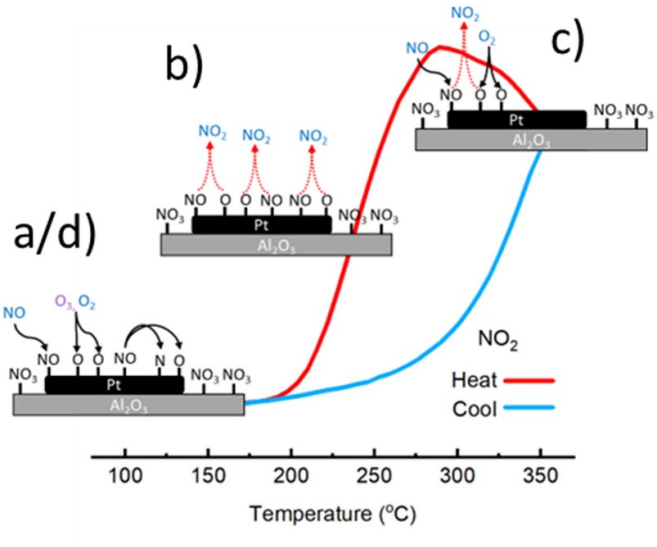

Figure 17. Diagram of the dominant surface processes taking place on Pt-Al_2O_3 during thermal cycling under plasma exposure. (a) NO, O_3 and O_2 adsorb at low temperature and are stored as Pt-NO and Pt-O. NO may also be lost (b) As the temperature increases, surface NO and O react to form NO_2 and desorb. (c) Depletion of reactants. Oxidation becomes dependent on immediate flux to the surface. (d) The catalyst returns to low temperature (a).

5. Conclusion

In this work, an evaluation of the interaction of an N_2/O_2/Ar APPJ with a downstream Pt-Al_2O_3 catalyst was explored. Both surface and downstream product characterization were compared to evaluate the effectiveness of the plasma–catalyst coupling. We record an enhancement of NO oxidation with plasma and catalyst vs the plasma alone or plasma plus bare support material at 350 °C. This is attributed to the oxidative ability of Pt, which increases the total oxygen present in downstream products at high temperatures compared to Al_2O_3. The change in O/N ratio of the products at 100 °C and 350 °C, for N_2 rich plasma, is 1.1–1.2 for Pt-Al_2O_3 and 1.2–1.0 for Al_2O_3. As short-lived reactive species such as O or N are likely quenched before reaching the catalyst surface, total NO_x production is mostly unchanged from the presence of Pt-Al_2O_3 or Al_2O_3. The differences in total NO_x that do occur may be due to destruction of plasma produced NO rather that additional NO formation.

By thermal cycling the catalyst under plasma exposure, the contributions of the surface and plasma to the overall reaction could be isolated. Thermal cycling results in a hysteresis pattern with elevated product formation at high temperatures. This hysteresis is a transient change and not the result of catalyst activation. This pattern is primarily due to NO_x storage at low temperatures which then reacts upon temperature increase. Surface analysis demonstrates that the change in intensity of Pt-NO during thermal cycling correlates best to downstream gas data. No other surface species have a marked decrease during heating to suggest desorption or reaction. However further analysis and comparison with the literature results in an unclear picture of which surface species is responsible for NO_x storage in this system. Two overlapping NO oxidation pathways exist during thermal cycling. One is due to steady state oxidation at high temperature, and the other due to oxidation of stored reactant species.

Primary reactive species fluxes to the surface are assessed to be NO and O_3. Increasing O_3 flux to the surface at low temperatures enhances oxidation at high temperatures. Pt-O surface coverage appears to be key to maintaining a high oxidation percentage but is quickly depleted. Looking forward, the ability to separate the effects of plasma and catalyst for systems where complex reactions and long-lasting surface changes may be taking place will be useful for the analysis and development of many reactions. Other observations make it clear that great care must be taken for correlation of product and surface analysis, which may be obscured due to gradients of adsorbed surface species throughout the catalyst powder bed.

The results presented in this work may be promising for tuning the downstream species for N_2/O_2 plasma catalyst coupling. They also represent an effective experimental approach for isolating the effects of plasma and catalyst in a coupled system. We are hopeful that these principles can be applied to other plasma catalytic mechanisms in the future.

Data availability statements

The data cannot be made publicly available upon publication because they are not available in a format that is sufficiently accessible or reusable by other researchers. The data that support the findings of this study are available upon reasonable request from the authors.

Acknowledgments

This material is based upon work supported by the U.S. Department of Energy, Office of Science, Office of Fusion Energy Sciences under award number DE-SC0020232. We thank Dr Peter Bruggeman, Dr Aditya Bhan, Brian Bayer, Audrey Fehlhaber, Yudong Li, Dr Shiqiang Zhang, and Sang-Jin Chung for helpful discussions and contributions to this work.

ORCID iDs

Michael Hinshelwood https://orcid.org/0009-0008-5808-8830
Gottlieb S Oehrlein https://orcid.org/0000-0002-6693-4274

References

[1] Winter L R and Chen J G 2021 N_2 fixation by plasma-activated processes *Joule* **5** 300–15
[2] Lee B, Winter L R, Lee H, Lim D, Lim H and Elimelech M 2022 Pathways to a green ammonia future *ACS Energy Lett.* **7** 3032–8
[3] Zhang L, Ji X, Ren X, Luo Y, Shi X, Asiri A M, Zheng B and Sun X 2018 Efficient electrochemical N_2 reduction to NH_3

on MoN nanosheets array under ambient conditions *ACS Sustain. Chem. Eng.* **6** 9550–4
[4] Zhu X, Mou S, Peng Q, Liu Q, Luo Y, Chen G, Gao S and Sun X 2020 Aqueous electrocatalytic N 2 reduction for ambient NH 3 synthesis: recent advances in catalyst development and performance improvement *J. Mater. Chem.* A **8** 1545–56
[5] Vu M H, Sakar M and Do T O 2018 Insights into the recent progress and advanced materials for photocatalytic nitrogen fixation for ammonia (NH_3) production *Catalysts* **8** 621
[6] Bogaerts A*et al* 2020 The 2020 plasma catalysis roadmap *J. Phys. D: Appl. Phys.* **53** 443001
[7] Talebizadeh P, Babaie M, Brown R, Rahimzadeh H, Ristovski Z and Arai M 2014 The role of non-thermal plasma technique in NO_x treatment: a review *Renew. Sustain. Energy Rev.* **40** 886–901
[8] Li Y, Jiang J, Hinshelwood M, Zhang S, Bruggeman P J and Oehrlein G S 2022 Characterization of plasma catalytic decomposition of methane: role of atomic O and reaction mechanism *J. Phys. D: Appl. Phys.* **55** 155204
[9] Whitehead J C 2016 Plasma–catalysis: the known knowns, the known unknowns and the unknown unknowns *J. Phys. D: Appl. Phys.* **49** 243001
[10] Tendero C, Tixier C, Tristant P, Desmaison J and Leprince P 2006 Atmospheric pressure plasmas: a review *Spectrochim. Acta* B **61** 2–30
[11] Winter L R, Ashford B, Hong J, Murphy A B and Chen J G 2020 Identifying surface reaction intermediates in plasma catalytic ammonia synthesis *ACS Catal.* **10** 14763–74
[12] Wang Z, Zhang Y, Neyts E C, Cao X, Zhang X, Jang B W L and Liu C-J 2018 Catalyst preparation with plasmas: how does it work? *ACS Catal.* **8** 2093–110
[13] Li Y, Hinshelwood M and Oehrlein G S 2022 Investigation of Ni catalyst activation during plasma-assisted methane oxidation *J. Phys. D: Appl. Phys.* **55** 155202
[14] Rouwenhorst K H, Engelmann Y, van't Veer K, Postma R S, Bogaerts A and Lefferts L 2020 Plasma-driven catalysis: green ammonia synthesis with intermittent electricity *Green Chem.* **22** 6258–87
[15] Rouwenhorst K H, Jardali F, Bogaerts A and Lefferts L 2021 From the Birkeland–Eyde process towards energy-efficient plasma-based NO_X synthesis: a techno-economic analysis *Energy Environ. Sci.* **14** 2520–34
[16] Vervloessem E, Aghaei M, Jardali F, Hafezkhiabani N and Bogaerts A 2020 Plasma-based N_2 fixation into NO_x: insights from modeling toward optimum yields and energy costs in a gliding arc plasmatron *ACS Sustain. Chem. Eng.* **8** 9711–20
[17] Jardali F, Alphen S V, Creel J, Eshtehardi H A, Axelsson M, Ingels R, Snyders R and Bogaerts A 2021 NO_x production in a rotating gliding arc plasma: potential avenue for sustainable nitrogen fixation *Green Chem.* **23** 1748–57
[18] Pei X, Gidon D, Yang Y J, Xiong Z and Graves D B 2019 Reducing energy cost of NO_x production in air plasmas *Chem. Eng. J.* **362** 217–28
[19] Ma H, Sharma R K, Welzel S, van de Sanden M C M, Tsampas M N and Schneider W F 2022 Observation and rationalization of nitrogen oxidation enabled only by coupled plasma and catalyst *Nat. Commun.* **13** 402
[20] Patil B S, Cherkasov N, Lang J, Ibhadon A O, Hessel V and Wang Q 2016 Low temperature plasma-catalytic NO_x synthesis in a packed DBD reactor: effect of support materials and supported active metal oxides *Appl. Catal.* B **194** 123–33
[21] Zhang S and Oehrlein G S 2021 From thermal catalysis to plasma catalysis: a review of surface processes and their characterizations *J. Phys. D: Appl. Phys.* **54** 213001
[22] Knoll A J, Zhang S, Lai M, Luan P and Oehrlein G S 2019 Infrared studies of gas phase and surface processes of the enhancement of catalytic methane decomposition by low temperature plasma *J. Phys. D: Appl. Phys.* **52** 225201
[23] Zhang S, Sobota A, van Veldhuizen E M and Bruggeman P J 2015 Temporally resolved ozone distribution of a time modulated RF atmospheric pressure argon plasma jet: flow, chemical reaction, and transient vortex *Plasma Sources Sci. Technol.* **24** 045015
[24] Hofmann S, van Gessel A F H, Verreycken T and Bruggeman P 2011 Power dissipation, gas temperatures and electron densities of cold atmospheric pressure helium and argon RF plasma jets *Plasma Sources Sci. Technol.* **20** 065010
[25] Gaens W V, Bruggeman P J and Bogaerts A 2014 Numerical analysis of the NO and O generation mechanism in a needle-type plasma jet *New J. Phys.* **16** 063054
[26] Chen X, Huo X, Liu J, Wang Y, Werth C J and Strathmann T J 2017 Exploring beyond palladium: catalytic reduction of aqueous oxyanion pollutants with alternative platinum group metals and new mechanistic implications *Chem. Eng. J.* **313** 745–52
[27] Engelbrecht N, Chiuta S and Bessarabov D G 2018 A highly efficient autothermal microchannel reactor for ammonia decomposition: analysis of hydrogen production in transient and steady-state regimes *J. Power Sources* **386** 47–55
[28] Gordon I E, Rothman L S, Hill C, Kochanov R V, Tan Y and Bernath P F 2017 The HITRAN2016 molecular spectroscopic database *J. Quant. Spectrosc. Radiat. Transfer* **203** 3–69
[29] Bartlett R W 1967 Platinum oxidation kinetics with convective diffusion and surface reaction *J. Electrochem. Soc.* **114** 547
[30] Johnson Matthey M J Technology review *The Oxidation of the Platinum Metals* (available at: www.technology.matthey.com/article/19/4/135-140/) (Accessed 11 October 2021)
[31] Plessow P N and Abild-Pedersen F 2016 Sintering of Pt nanoparticles via volatile PtO_2: simulation and comparison with experiments *ACS Catal.* **6** 7098–108
[32] Yeo C D, He M, Lee J, Shah N M R, Hong Y K, Choi M, You J H, Purani D and Lee J K 2020 Recovering magnetic domains of nanoscale-mechanically damaged ferromagnetic thin film of information data storage *Appl. Mater. Today* **21** 100825
[33] Olsson L, Westerberg B, Persson H, Fridell E, Skoglundh M, Andersson B and Kinetic A 1999 Study of oxygen adsorption/desorption and NO oxidation over Pt/Al_2O_3 catalysts *J. Phys. Chem.* B **103** 10433–9
[34] Wright A M, Sun C and Dincă M 2021 Thermal Cycling of a MOF-Based NO Disproportionation Catalyst *J. Am. Chem. Soc.* **143** 681–6
[35] Hinshelwood M and Oehrlein G S 2024 in preparation
[36] Bradford M C J and Vannice M A 1998 CO_2 Reforming of CH_4 over supported Pt catalysts *J. Catal.* **173** 157–71
[37] Vaarkamp M, Miller J T, Modica F S and Koningsberger D C 1996 On the relation between particle morphology, structure of the metal-support interface, and catalytic properties of $Pt/\gamma\text{-}Al_2O_3$ *J. Catal.* **163** 294–305
[38] Zhang Z, He G, Li Y, Zhang C, Ma J and He H 2022 Effect of hydroxyl groups on metal anchoring and formaldehyde oxidation performance of Pt/Al_2O_3 *Environ. Sci. Technol.* **56** 10916–24
[39] Ingelsten H H, Hellman A, Kannisto H and Grönbeck H 2009 Experimental and theoretical characterization of NO_x species on $Ag/\alpha\text{-}Al_2O_3$ *J. Mol. Catal. Chem.* **314** 102–9

[40] O'Brien C P and Lee I C 2017 A detailed spectroscopic analysis of the growth of oxy-carbon species on the surface of Pt/Al_2O_3 during propane oxidation *J. Catal.* **347** 1–8
[41] Aguirre A and Collins S E 2019 Insight into the mechanism of acetonitrile hydrogenation in liquid phase on Pt/Al_2O_3 by ATR-FTIR *Catal. Today* **336** 22–32
[42] Kahsar K R, Schwartz D K and Medlin J W 2015 Stability of self-assembled monolayer coated Pt/Al_2O_3 catalysts for liquid phase hydrogenation *J. Mol. Catal. Chem.* **396** 188–95
[43] Yu Y, He H, Feng Q, Gao H and Yang X 2004 Mechanism of the selective catalytic reduction of NO_x by C_2H_5OH over Ag/Al_2O_3 *Appl. Catal.* B **49** 159–71
[44] Yu S, Niu X, Song Z, Huang X, Peng Y and Li J 2022 Improvement of Al_2O_3 on the multi-pollutant control performance of NO_x and chlorobenzene in vanadia-based catalysts *Chemosphere* **289** 133156
[45] Toops T J, Smith D B, Epling W S, Parks J E and Partridge W P 2005 Quantified NO_x adsorption on Pt/K/gamma-Al_2O_3 and the effects of CO_2 and H_2O *Appl. Catal.* B **58** 255–64
[46] Toops T J, Smith D B and Partridge W P 2005 Quantification of the in situ DRIFT spectra of Pt/K/γ-$A1_2O_3$ NO_x adsorber catalysts *Appl. Catal.* B **58** 245–54
[47] Ottinger N A, Toops T J, Nguyen K, Bunting B G and Howe J 2011 Effect of lean/rich high temperature aging on NO oxidation and NO_x storage/release of a fully formulated lean NO_x trap *Appl. Catal.* B **101** 486–94
[48] Ji Y, Bai S and Crocker M 2015 Al_2O_3-based passive NO_x adsorbers for low temperature applications *Appl. Catal.* B **170–171** 283–92
[49] Baltrusaitis J, Schuttlefield J, Jensen J H and Grassian V H 2007 FTIR spectroscopy combined with quantum chemical calculations to investigate adsorbed nitrate on aluminium oxide surfaces in the presence and absence of co-adsorbed water *Phys. Chem. Chem. Phys.* **9** 4970–80
[50] Pieta I S, García-Diéguez M, Herrera C, Larrubia M A and Alemany L J 2010 In situ DRIFT–TRM study of simultaneous NO_x and soot removal over Pt–Ba and Pt–K NSR catalysts *J. Catal.* **270** 256–67
[51] Ma Q, Liu Y and He H 2008 Synergistic effect between NO_2 and SO_2 in their adsorption and reaction on γ-alumina *J. Phys. Chem.* A **112** 6630–5
[52] Gao X, Zhong C, Tang M, Ma Q and Liu C 2021 Key factors determining heterogeneous uptake kinetics of NO_2 onto alumina: implication for the linkage between laboratory work and modeling study *J. Geophys. Res. Atmos.* **126** e2021JD034694
[53] Du C, Kong L, Zhanzakova A, Tong S, Yang X, Wang L, Fu H, Cheng T, Chen J and Zhang S 2018 Impact of heterogeneous uptake of nitrogen dioxide on the conversion of acetaldehyde on gamma-alumina in the absence and presence of simulated solar irradiation *Atmos. Environ.* **187** 282–91
[54] Nova I, Castoldi L, Lietti L, Tronconi E, Forzatti P and Prinetto F 2004 NO_x adsorption study over Pt–Ba/alumina catalysts: FT-IR and pulse experiments *J. Catal.* **222** 377–88
[55] Ji Y, Toops T J, Pihl J A and Crocker M 2009 NO_x storage and reduction in model lean NO_x trap catalysts studied by in situ DRIFTS *Appl. Catal.* B **91** 329–38
[56] Westerberg B and Fridell E 2001 A transient FTIR study of species formed during NO_x storage in the $Pt/BaO/Al_2O_3$ system *J. Mol. Catal. Chem.* **165** 249–63
[57] Wakabayashi R, Tomita A and Kimura T 2020 Understanding of NO_x storage property of impregnated Ba species after crystallization of mesoporous alumina powders *J. Hazards Mater.* **398** 122791
[58] Castoldi L, Matarrese R, Morandi S, Righini L and Lietti L 2018 New insights on the adsorption, thermal decomposition and reduction of NO_x over Pt- and Ba-based catalysts *Appl. Catal.* B **224** 249–63
[59] Sedlmair C, Seshan K, Jentys A and Lercher J A 2003 Elementary steps of NO_x adsorption and surface reaction on a commercial storage–reduction catalyst *J. Catal.* **214** 308–16
[60] Narula C K, Allard L F, Stocks G M and Moses-debusk M 2014 Remarkable NO oxidation on single supported platinum atoms *Sci. Rep.* **4** 7238
[61] Wang C, Kong L, Jin S, Xia L, Tan J and Wang Y 2022 Effect of diesel soot on the heterogeneous reaction of NO_2 on the surface of γ-Al_2O_3 *Atmosphere* **13** 333
[62] Gaens W V, Iseni S, Schmidt-Bleker A, Weltmann K D, Reuter S and Bogaerts A 2015 Numerical analysis of the effect of nitrogen and oxygen admixtures on the chemistry of an argon plasma jet operating at atmospheric pressure *New J. Phys.* **17** 033003
[63] van Gessel A F H, Alards K M J and Bruggeman P J 2013 NO production in an RF plasma jet at atmospheric pressure *J. Phys. D: Appl. Phys.* **46** 265202
[64] Gaens W V and Bogaerts A 2013 Kinetic modelling for an atmospheric pressure argon plasma jet in humid air *J. Phys. D: Appl. Phys.* **46** 275201
[65] Schmidt-Bleker A, Bansemer R, Reuter S and Weltmann K D 2016 How to produce an NO_x- instead of O_x-based chemistry with a cold atmospheric plasma jet *Plasma Process. Polym.* **13** 1120–7
[66] Shimizu T, Sakiyama Y, Graves D B, Zimmermann J L and Morfill G E 2012 The dynamics of ozone generation and mode transition in air surface micro-discharge plasma at atmospheric pressure *New J. Phys.* **14** 103028
[67] Bourges P, Lunati S and Mabilon G 1998 N_2O and NO_2 formation during NO reduction on precious metal catalysts *Studies in Surface Science and Catalysis* (*Catalysis and Automotive Pollution Control IV* vol 116) ed N Kruse, A Frennet and J M Bastin (Elsevier) pp 213–22 (available at: www.sciencedirect.com/science/article/pii/S0167299198808781)
[68] Wan S, Keller K, Lott P, Bhimrao Shirsath A, Tischer S, Häber T, Suntz R and Deutschmann O 2022 Experimental and numerical investigation of NO oxidation on Pt/Al_2O_3—and NO_x storage on $Pt/BaO/Al_2O_3$-catalysts *Catal. Sci. Technol.* **12** 4456–70
[69] Arevalo R L, Escaño M C S and Kasai H 2015 First-principles study of nitric oxide oxidation on Pt(111) versus Pt overlayer on 3d transition metals *J. Vac. Sci. Technol.* A **33** 021402
[70] Wu L, Tong S and Ge M 2013 Heterogeneous reaction of NO_2 on Al_2O_3: the effect of temperature on the nitrite and nitrate formation *J. Phys. Chem.* A **117** 4937–44
[71] Gao B, Zhang N, Zhang H, Qiu R, Chen Z, Li Y and Yang Z 2022 Effects of platinum high-temperature redispersion on Pt/Al_2O_3 diesel oxidation catalyst for nitric oxide oxidation and its reaction pathway *J. Environ. Chem. Eng.* **10** 108669
[72] Castoldi L, Righini L, Matarrese R, Lietti L and Forzatti P 2015 Mechanistic aspects of the release and the reduction of NO_x stored on Pt–Ba/Al_2O_3 *J. Catal.* **328** 270–9
[73] De Abreu Goes J E, Kristoffersson A and Olsson L 2019 Sulfur poisoning effects on modern lean NO_x trap catalysts components *Catalysts* **9** 492
[74] Olsson L, Persson H, Fridell E, Skoglundh M, Andersson B and Kinetic A 2001 Study of NO oxidation and NO_x storage on Pt/Al_2O_3 and $Pt/BaO/Al_2O_3$ *J. Phys. Chem.* B **105** 6895–906
[75] Crocoll M, Kureti S and Weisweiler W 2005 Mean field modeling of NO oxidation over Pt/Al_2O_3 catalyst under oxygen-rich conditions *J. Catal.* **229** 480–9

[76] Salman A U R, Enger B C, Auvray X, Lødeng R, Menon M, Waller D and Rønning M 2018 Catalytic oxidation of NO to NO_2 for nitric acid production over a Pt/Al_2O_3 catalyst *Appl. Catal. Gen.* **564** 142–6

[77] Benard S, Retailleau L, Gaillard F, Vernoux P and Giroir-Fendler A 2005 Supported platinum catalysts for nitrogen oxide sensors *Appl. Catal.* B **55** 11–21

[78] Mulla S S, Chen N, Cumaranatunge L, Blau G E, Zemlyanov D Y, Delgass W N, EPLING W and Ribeiro F 2006 Reaction of NO and O_2 to NO_2 on Pt: kinetics and catalyst deactivation *J. Catal.* **241** 389–99

[79] Uy D, O'Neill A E and Weber W H 2002 UV Raman studies of adsorbed oxygen and NO_x species on Pt/γ-alumina catalysts *Appl. Catal.* B **35** 219–25